REVIEW OF EXPERIMENTAL RESULTS IN ELECTROPRODUCTION

By K. Berkelman

Laboratory of Nuclear Studies, Cornell University, Ithaca, New York 14850, USA*

(Presented at the XIV Cracow School of Theoretical Physics, Zakopane, June 15–28, 1974)

I will summarize the available data on hadronic final states in high-energy electron--nucleon scattering, with emphasis on the most recent experiments in the deep inelastic scaling region.

CONTENTS

A. Introduction

1. Scope of these lectures

My purpose is to review for you what we have learned from experiment about hadronic final states in inelastic electron scattering. Since this audience is mainly theorists, I will concentrate on the results of the experiments and will discuss the technical details only

* Address from July, 1974 to July, 1975: DESY, Notkestieg 1, 2 Hamburg 52, Germany, Federal Republic.

enough to explain why the regions of experimental and theoretical activity overlap so little. On the other hand, I will try not to tie the discussiontoo closely to particular theoretical models; I will attempt to keep an unbiased point of view.

Let me apologize for the fact that this is not a comprehensive review, but only a personal sampling of what I think is significant. More details can be found in the reviews by Brasse [1], Talman [2], Meyer [3], and Clegg [4] at the Bonn conference (August, 1973), and in more recent papers [5, 6].

2. Kinematics

You are all familiar with the results [7] from single-arm inelastic electron scattering, but I still have to say something about them in order to set the stage for what will follow. The term "single-arm" refers to the fact that only the scattered electron is detected in a single spectrometer; the hadron final state is not observed. From the measured laboratory incident and scattered energies E and E' and scattering angle θ we can construct three independent variables on which the experimental cross section can depend: for instance,

(1) the invariant four-momentum transfer squared

$$q^2 = (p_e - p_e')^2 = -4EE' \sin^2 \frac{\theta}{2}$$

(experimenters use $Q^2 = -q^2 > 0$),

(2) the invariant mass-squared of the hadronic final state

$$W^2 = (p_p + q)^2 = 2M(E-E') + M^2 - Q^2 = s$$

(often the invariant $\nu = p_p \cdot q/M = E - E'$ is used instead),

(3) the virtual photon polarization parameter

$$\varepsilon = \left[1 + 2\,\frac{Q^2+\nu^2}{Q^2} \tan^2 \frac{\theta}{2}\right]^{-1}.$$

If we assume that the cross section is dominated by the exchange of a single photon, we can express it in terms of two structure functions depending on the *two* variables Q^2 and W (or ν):

$$\frac{d\sigma}{d\Omega dE'} = \frac{4\alpha^2 E'^2}{Q^4}\left[W_2 \cos^2 \frac{\theta}{2} + 2W_1 \sin^2 \frac{\theta}{2}\right].$$

From the single-arm experiments at SLAC [7], we learn, however, that it is even simpler than that. Over a wide range ($W > 2\,\text{GeV}$, $Q^2 > 2\,\text{GeV}^2$) the structure functions νW_2 and W_1 apparently depend only on the ratio W^2/Q^2. As you know, this scaling property is responsible for much of the theoretical activity in recent years. If the most naive picture is correct, that the structure functions scale because the nucleon is composed of pointlike constituents, then we have here a unique probe of the fundamental structure of hadrons.

There is now evidence from a Cornell, Michigan-State, San-Diego experiment, using a high energy μ beam at N. A. L., that scaling breaks down above $Q^2 = 40$ GeV^2. Since these data are rather new, I will say no more about them. Such a scaling violation is irrelevant anyway, since all the data I will show you on the hadronic final states come from much lower Q^2.

3. Experimental techniques

The coincidence electroproduction experiments that I am going to discuss have been carried out at five electron accelerators: SLAC (20 GeV), Cornell (12 GeV), DESY (7 GeV), CEA (5 GeV, before it was shut down), and NINA (4 GeV). A wide variety of techniques have been used.

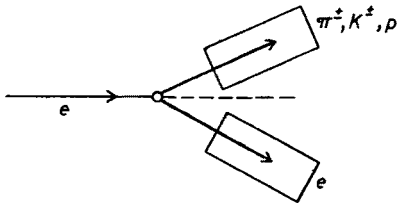

(a) Two high-resolution magnetic spectrometers, to observe in coincidence the scattered electron and one charged hadron emitted at a relatively small angle: CEA and Cornell (Pipkin et al. [5, 8]), DESY (Brasse et al. [9] and Schmidt et al. [10]), NINA (Ibbotson et al. [11]).

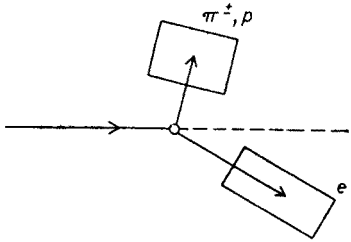

(b) The same technique, but with the hadron spectrometer designed for lower momentum and larger aperture, and positioned at larger angles to the beam: SLAC (Bloom et al. [12]), Cornell (Cassel et al. [13] and Talman et al. [14]).

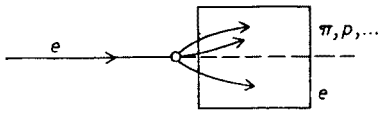

(c) One spectrometer in the forward direction with large enough aperture to detect the scattered electron and one or several hadrons from the same event: SLAC (Perl et al. [15]).

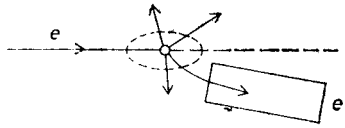

(d) A spectrometer for the scattered electrons in coincidence with a scintillation counter array surrounding the target: Cornell (Berkelman et al. [6]).

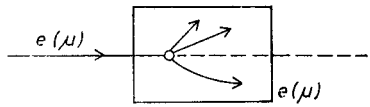

(e) A track chamber surrounding the electroproduction vertex: SLAC (Ballam et al. [16] — rapid-cycling triggered hydrogen bubble chamber), DESY (Meyer et al. [17] — streamer chamber).

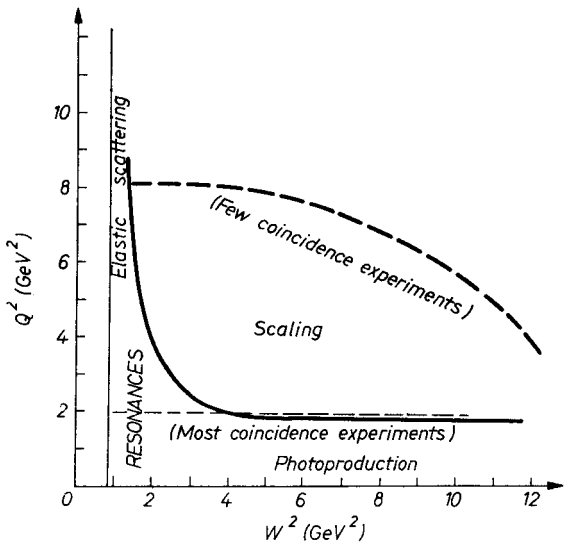

Fig. 1. A part of the Q^2, W^2 plane, showing the region covered by coincidence electroproduction experiments

Fig. 1 shows a part of the Q^2, W^2 plane, indicating approximately the region investigated so far, more or less thoroughly, by the coincidence experiments in which one or more of the final state hadrons is observed along with the scattered electron. It is only a small part of the range covered in the single-arm experiments, and certainly an even smaller part of the range covered in the usual theory papers, in which Q^2 and ν are each taken to infinity. The limitation in W is a kinematic limit coming from the available beam energy in electron accelerators. The Q^2 limit, however, is a rate limit. The electron-hadron

coincidence counting rate R_{co} is proportional to the scattering cross section, which contains the factor Q^{-4}, and to the beam intensity I, among other factors:

$$R_{co} \propto I/Q^4.$$

The accidental random coincidence rate is proportional to the product of the separate counting rates in the electron and hadron detectors, and is therefore proportional to the square of the beam intensity:

$$R_{acc} \propto I^2.$$

In the *single*-arm experiments, one has been able to compensate for the Q^{-4} factor in the data rate by increasing the beam intensity for the high Q^2 measurements. In the *coincidence* experiments, however, as one increases I one eventually reaches the situation in which the random coincidences significantly contaminate the true coincidence measurement, making it impossible to determine the coincidence cross section at higher Q^2. This difficulty is common to all experimental techniques, but is especially severe in the track chamber experiments, and at low duty-cycle accelerators (such as the SLAC linac).

B. The Resonance Region: $W < 2$ GeV

1. Results from single-arm experiments

As in photoproduction, the electroproduction cross section below $W \approx 2$ GeV is dominated (see Fig. 2) by excitation of nucleon resonances: $e+N \to e + N^*$. The resemblance is not surprising, since the electroproduction can be viewed as photoproduction by

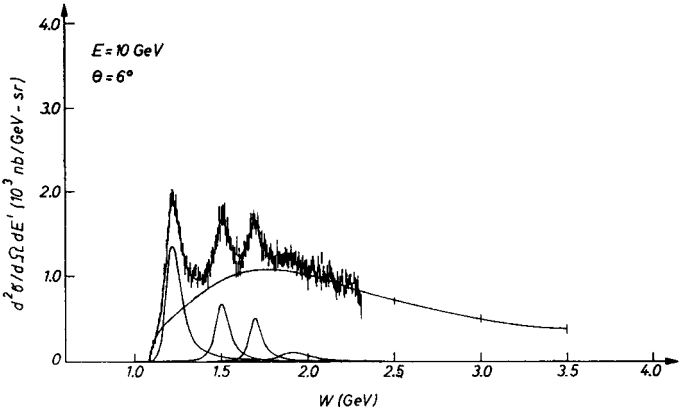

Fig. 2. A typical momentum spectrum [7] of electrons scattered at fixed incident energy and scattering angle, in the resonance region. The curves show fits to the resonances

off-mass-shell polarized photons. To make the analogy more explicit, we express the single-arm electron scattering cross section in terms of cross sections for absorption of transversely and longitudinally polarized photons, instead of in terms of the structure functions W_1 and W_2:

$$\frac{d\sigma}{d\Omega dE'} = \Gamma(\sigma_T + \varepsilon\sigma_L),$$

where

$$\Gamma = \frac{\alpha}{2\pi^2}\,\frac{E'}{E}\,\frac{W^2-M^2}{2MQ^2}\,\frac{1}{1-\varepsilon},$$

and σ_T and σ_L are functions of W and Q^2. In the limit $Q^2 \to 0$ we have $\sigma_T(W, Q^2) \to \sigma_\gamma(W)$ and $\sigma_L \to O(Q^2)$.

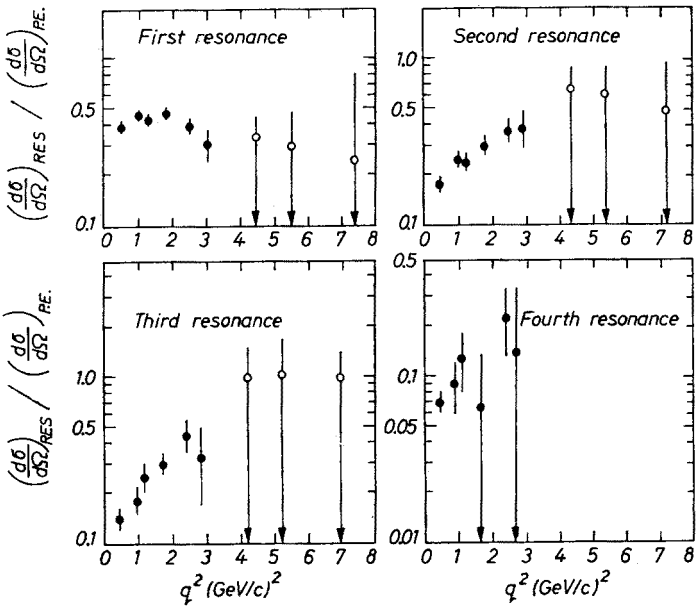

Fig. 3. The ratio of resonance and elastic cross sections [7] versus Q^2

The W dependence of σ_T and σ_L at fixed Q^2 shows qualitatively the same resonance behaviour as does the photoproduction cross section σ_γ. The Q^2 dependence turns out to be similar to the rather rapid falloff in elastic scattering (see Fig. 3). The structure function for elastic scattering can be written as

$$\nu W_2 = \frac{Q^2}{2M}\,\frac{G_E^2 + (Q^2/4M^2)G_M^2}{1+(Q^2/4M^2)}\,\delta(W-M)$$

and since $G_M \propto G_E \approx (1+Q^2/0.71)^{-2}$, it is clear that at high Q^2 the elastic (and resonance) structure function decreases as Q^{-6}, and the corresponding $\sigma_T+\sigma_L$ decreases as Q^{-8}.

2. Coincidence results on $e+p \to e+\Delta(1236)$

Actually the cross sections for the production of the various nucleon resonances depend on their effective transition form factors $G^i_{\gamma NN^*}(Q^2)$. The index i distinguishes the

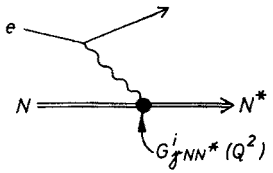

three (in general) form factors for a given resonance. We can parametrize the $\gamma p\Delta^+(1236)$ vertex with three form factors, $G^M_{\gamma p\Delta}$, $G^E_{\gamma p\Delta}$ and $G^L_{\gamma p\Delta}$, corresponding to the magnetic dipole, electric quadrupole, and longitudinal quadrupole excitation amplitudes.

In order to measure separately the three form factors for each resonance, as well as to resolve the resonance contribution cleanly from other contributions, one must look at the hadronic final state — separate the isobar decay channels and observe the angular distributions and perhaps polarizations. At this point we have to take into account the fact that the virtual photon is polarized transversely and longitudinally. This causes in the final states an azimuthal asymmetry about the virtual photon axis, constrained to be of the form

$$\frac{d\sigma}{d\Omega_h d\Omega_e dE'} = \Gamma\left(\frac{d\sigma_u}{d\Omega_h} + \varepsilon\frac{d\sigma_L}{d\Omega_h} + \varepsilon\frac{d\sigma_p}{d\Omega_h}\cos 2\varphi + \sqrt{\varepsilon(\varepsilon+1)}\frac{d\sigma_I}{d\Omega_h}\cos\varphi\right),$$

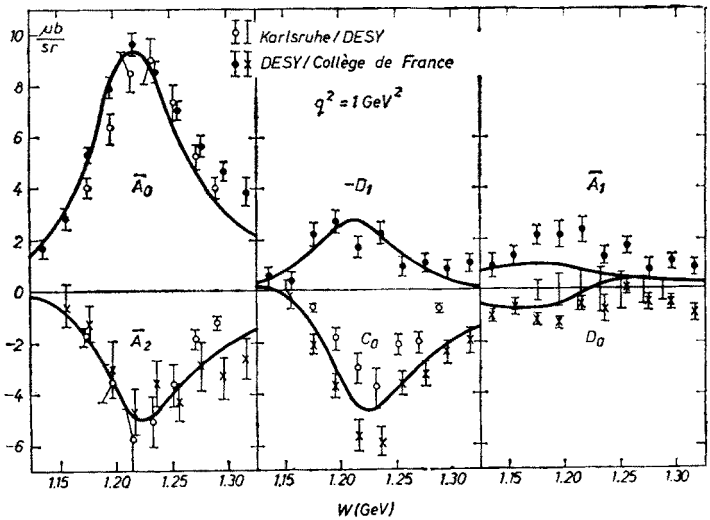

Fig. 4. DESY measurements [4] of the angular coefficients in $\gamma_V p \to \pi^0 p$ at the first resonance, plotted against W for $Q^2 = 1$ GeV^2

where the $d\sigma_u/d\Omega_h$, etc. are functions of W, Q^2, and the meson center-of-mass production angle. $d\sigma_u/d\Omega_h$ is the average differential cross section for the two transverse linear polarization states, and goes to the unpolarized photoproduction cross section in the $Q^2 \to 0$ limit; $d\sigma_p/d\Omega_h$ is the difference between cross sections for photons polarized parallel and perpendicular to the meson production plane; $d\sigma_L/d\Omega_h$ is the cross section for production

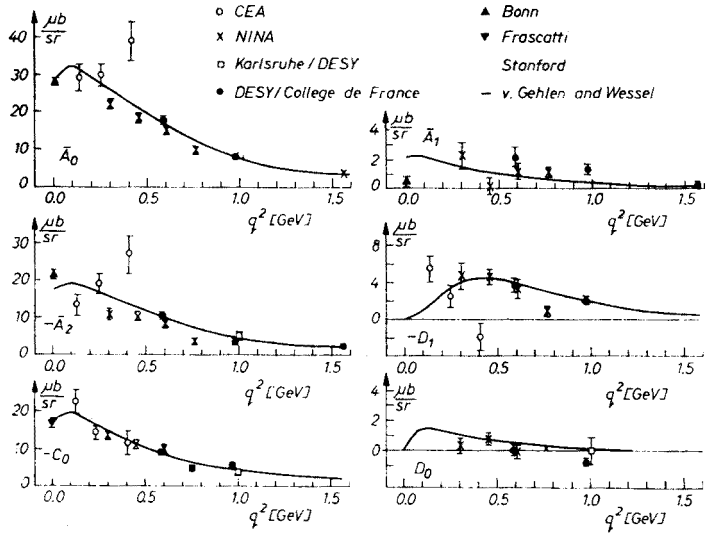

Fig. 5. Measurements [4] of the angular coefficients in $\gamma_V p \to \pi^0 p$ at the first resonance, plotted against Q^2

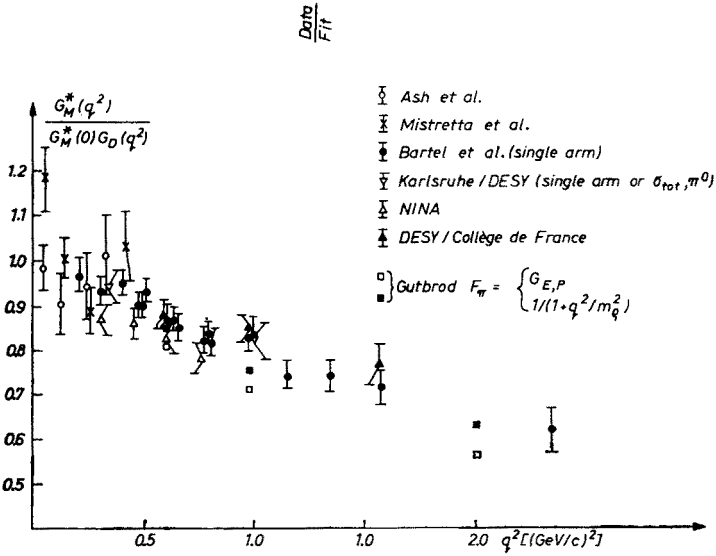

Fig. 6. Q^2 dependence [4] of the magnetic dipole $\gamma p \Delta$ transition form factor, divided by the elastic dipole form factor and normalized to 1 at $Q^2 = 0$

by longitudinally polarized photons; and $d\Omega_l/d\Omega_h$ arises from longitudinal-transverse interference. In principle, all four terms in the cross section can be separated experimentally, but the $d\sigma_u$ and $d\sigma_L$ separation is rather difficult and is not done in most experiments.

The detailed study of the final states has been carried out for the $\Delta^+(1236)$ in both the $n\pi^+$ and $p\pi^0$ channels at CEA (Wilson et al. [4]), DESY (Brasse et al. [4] and other

groups [4]), and NINA (Ibbotson et al. [4]). The data are usually plotted in terms of the Q^2 and W dependence of the coefficients in an expansion of each of the four cross section terms ($d\sigma_u/d\Omega_h$ and $\varepsilon d\sigma_L/d\Omega_h$ usually combined) in a power series in cos θ_h, truncated for s- and p-waves (see Figs 4 and 5):

$$\frac{d\sigma}{d\Omega_h d\Omega_e dE'} = \Gamma[\bar{A}_0 + \bar{A}_1 \cos\theta_h + \bar{A}_2 \cos^2\theta_h + \varepsilon C_0 \sin^2\theta_h \cos 2\varphi +$$

$$+ \sqrt{2\varepsilon(\varepsilon+1)}\,(D_0 + D_1 \cos\theta_h)\sin\theta_h \cos\varphi].$$

The strongest terms are $\bar{A}_0$, $\bar{A}_2$, and C_0, as one expects for dominance by the magnetic dipole amplitude. The $G^M_{\gamma p\Delta}$ form factor is therefore easily extracted (see Fig. 6). As in photoproduction, the electric quadrupole contribution is small. The D_1 term indicates a nonzero contribution from magnetic dipole interfering with longitudinal quadrupole. The size of the $G^L_{\gamma p\Delta}$ is interesting from the point of view of the quark model. These data have also been compared with extensions of the dispersion theoretic treatment of photoproduction.

3. Higher resonances etc.

A somewhat unrelated line of investigation, which nevertheless falls in this kinematic region, is the attempt to extract the axial form factor of the nucleon from the cross section

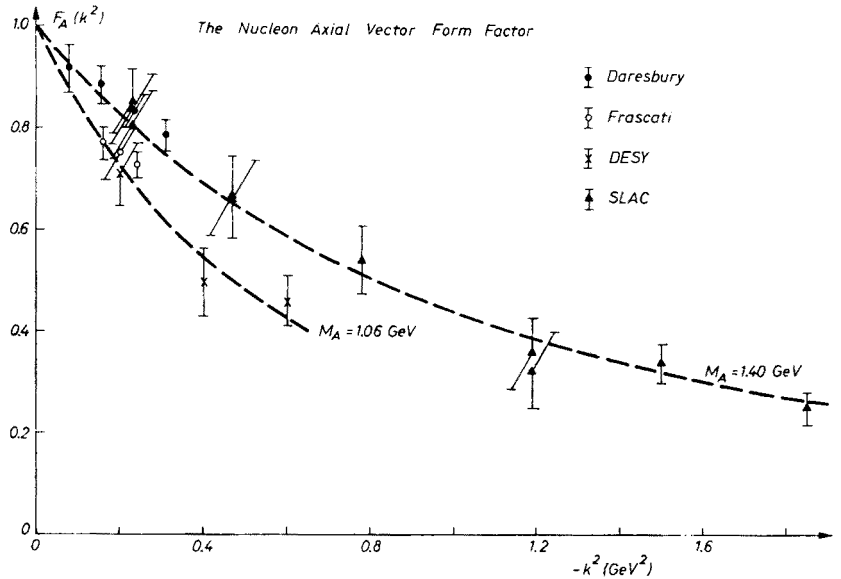

Fig. 7. Q^2 dependence [4] of the nucleon axial vector form factor, as derived from π^+n electroprouction experiments

for π^+ electroproduction near threshold. The analysis is strongly model-dependent and assumes PCAC, extrapolating to zero pion mass. The results are shown in Fig. 7. As a method of measuring the axial form factor, it is not as reliable as the neutrino experiments (summarized by Myatt in this series of lectures); at best it is a test of PCAC.

The detailed investigation of the "second resonance" at $W \approx 1500$ MeV has also begun. Since this probably involves several resonant states as well as partial waves beyond s and p, the analysis will be considerably more difficult. Fig. 8 shows data of the NINA group [4]. Another NINA group [4] has also measured η^0 production in the same energy range.

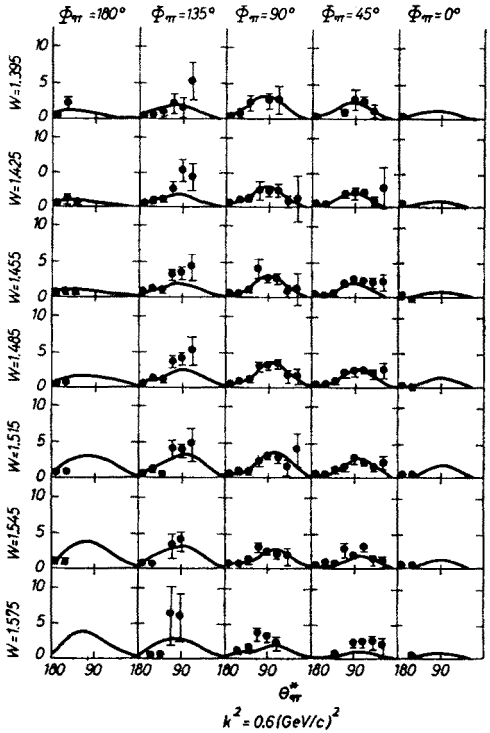

Fig. 8. Measurements [4] of the π^0p electroproduction cross section in the second resonance region, made at NINA

Although I have only briefly touched on the rather large body of data in the resonance region, I will summarize now, in order to leave time for discussion of the other regions of the Q^2, W^2 plane, which may be of more relevance to recent theoretical activity. The resonances have a W dependence like that of photoproduction, falling off rapidly in Q^2 like elastic scattering: $(\sigma_T+\sigma_L)_{res} \propto Q^{-8}$. The final states are the same as observed in photoproduction, the only unique feature being the contribution of longitudinal photons, which at least so far does not seem to be very strong.

C. The Low-Q^2 Transition Region: $Q^2 < 2 GeV^2$

1. Introduction

The scaling property of νW_2 and W_1 cannot possibly continue to hold in the low Q^2 limit. This is obvious from the relation between the structure functions and the virtual photon absorption cross section, for example,

$$W_2 = \frac{1}{4\pi^2\alpha}\,\frac{W^2-M^2}{2M}\,\frac{Q^2}{Q^2+\nu^2}\,(\sigma_T+\sigma_L),$$

and therefore for small Q^2,

$$\nu W_2 \approx \frac{Q^2}{4\pi^2\alpha}(\sigma_T+\sigma_L).$$

Since σ_T is finite in the $Q^2 \to 0$ limit, νW_2 must go to zero and cannot scale. At low Q^2 and fixed W the single-arm data [7] can be approximately fit by the form

$$\sigma_T+\sigma_L = \frac{\sigma_\gamma(W)}{1+Q^2/0.4},$$

a rather slow Q^2 dependence, which leads to a νW_2 which is independent of Q^2 at high Q^2 (keeping $Q^2 < W^2$, however). The low-Q^2 region is therefore a region of transition between photoproduction and the scaling region. The idea is to see how the final states in photoproduction are modified as the photon becomes more spacelike.

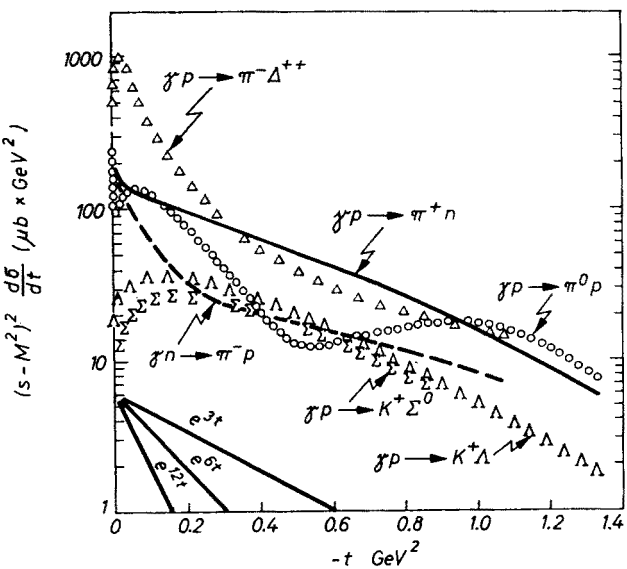

Fig. 9. A plot (from Diebold) of the t dependence of various non-diffractive photoproduction channels at high energies

To simplify the discussion I will divide the two-body channels into non-diffractive and diffractive categories. In photoproduction the non-diffractive processes are characterized by slow t dependence (Fig. 9) and rapid s fall off ($\propto (s-M^2)^{-2}$). The diffractive cross sections, however, fall off rapidly in t, (Fig. 10) and very slowly in s. The close similarity

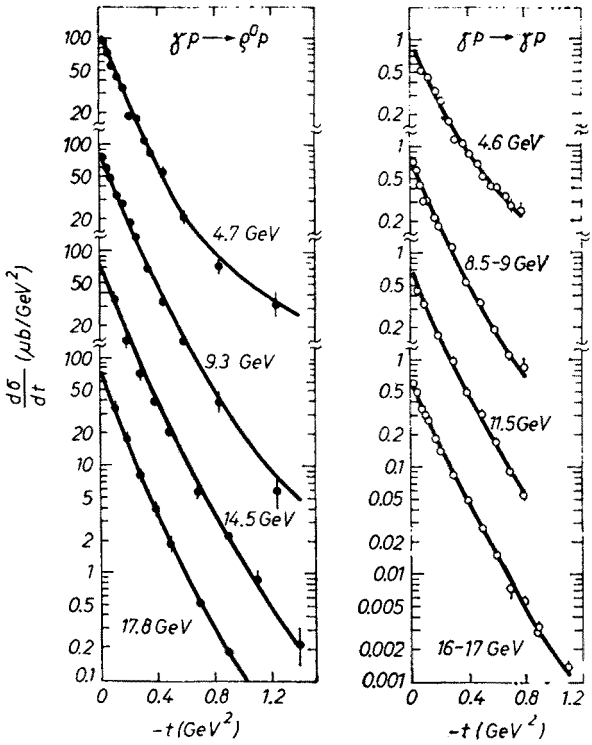

Fig. 10. SLAC data on ϱ^0 photoproduction and elastic γp scattering

between the behaviors of the vector meson photoproduction processes and of elastic γp scattering (Fig. 10) has inspired the vector-dominance model, in which the photon interacts with hadronic matter through vector meson intermediate states.

2. Non-diffractive two-body channels

In this category quite a few reactions have been investigated:

$$\begin{array}{ll} \gamma_V p \to \pi^+ n & \gamma_V n \to \pi^- p \\ \quad \pi^0 p & \quad \pi^- \Delta^+ \\ \quad \pi^+ \Delta^0 & \quad \pi^+ \Delta^-. \\ \quad \pi^- \Delta^{++} & \\ \quad K^+ \Lambda & \\ \quad K^+ \Sigma^0 & \\ \quad K^+ Y^{0*} & \end{array}$$

The experimental arrangement has always been the one denoted by (a) in Section A–3 above. The data come from CEA [8], Cornell [8], DESY [10], and NINA [11]. Fig. 11 shows a typical missing mass spectrum for the reaction $e+p \to e+\pi^+ +$ missing mass. Peaks corresponding to missing neutron and missing Δ^0 are easily distinguished; it is clear how

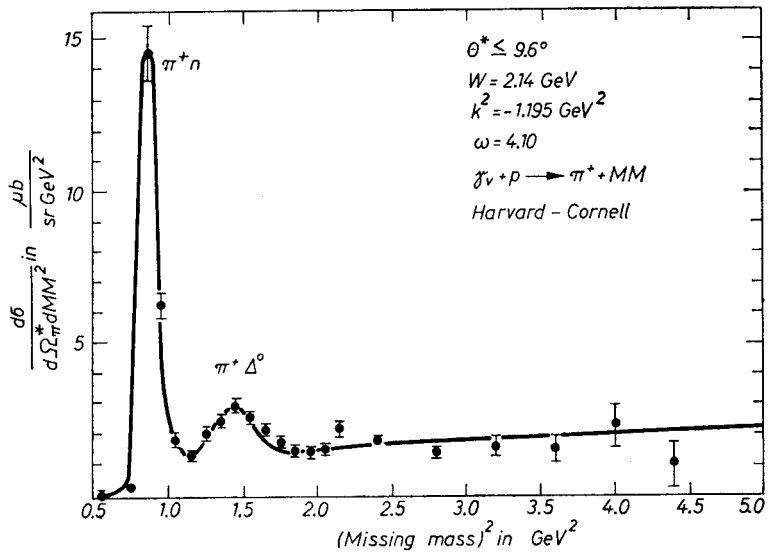

Fig. 11. A typical missing mass distribution obtained in a $e\pi^+$ coincidence electroproduction experiment [8]

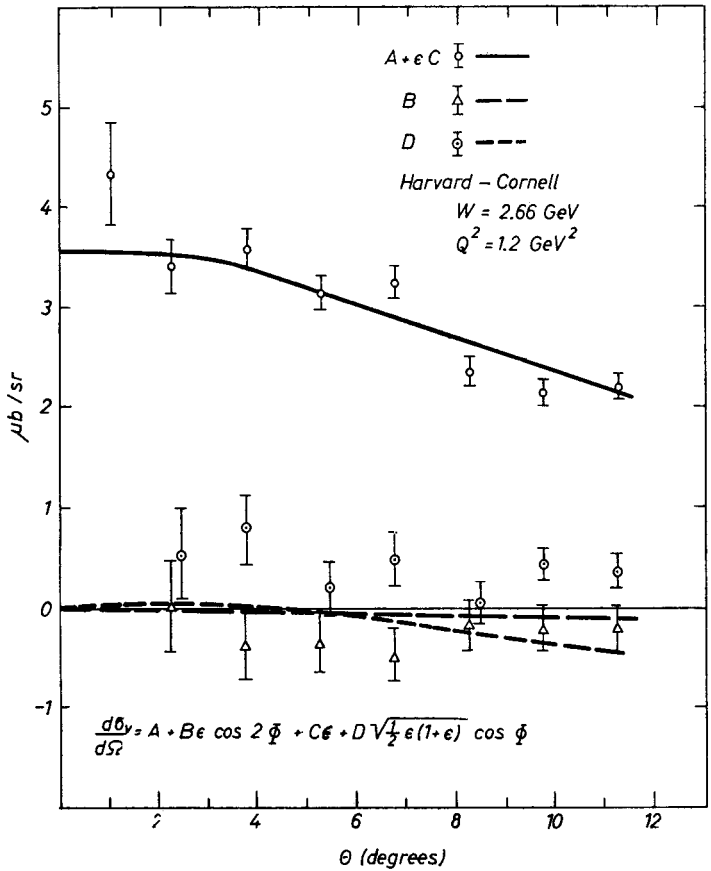

Fig. 12. Angular distributions of the various components of the cross section for $\gamma vp \rightarrow \pi^+ n$ at $W = 2.66$ GeV and $Q^2 = 1.2$ GeV^2, measured at Cornell [8]

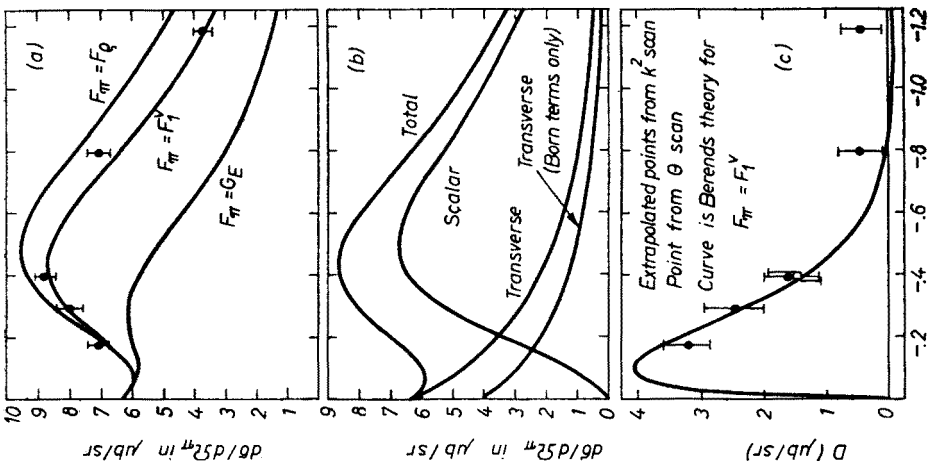

Fig. 14. CEA data [8] on the Q^2 dependence of π^+n electroproduction, compared with the electric Born model of Behrends [18]

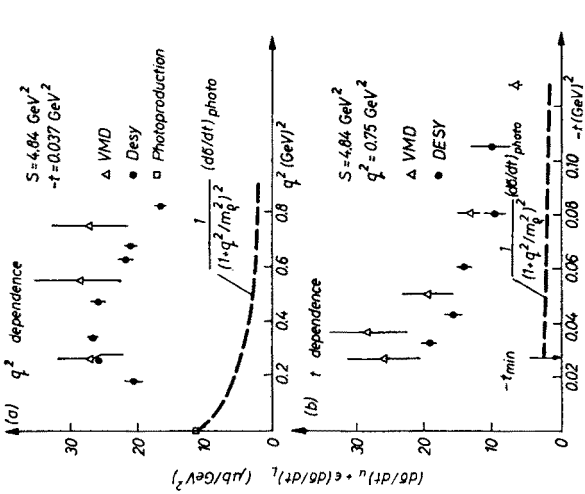

Fig. 13. DESY data [10] on the Q^2 and t dependence of the cross section for $\gamma^*p \to \pi^+n$

one extracts the corresponding π^+n and $\pi^+\Delta^0$ cross sections. I will discuss the π^+n channel in some detail and summarize briefly the others.

Figures 12 and 13 show a sampling of θ_π, t, and Q^2 dependences for $\gamma_V p \to \pi^+ n$. The data have been analyzed in terms of the electric Born model, essentially the three pole terms plus dispersion corrections [18]. An interesting feature of this model is the very

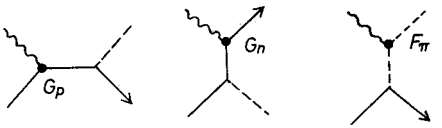

strong contribution of the longitudinal photon polarization component in the pion exchange amplitude (Fig. 14). The pion pole term is suppressed by angular momentum conservation in forward pion production by transverse photons, and therefore does not contribute strongly in ordinary photoproduction. The pion exchange amplitude contains the pion charge form factor, the only unknown in the model. Then, provided the model is correct,

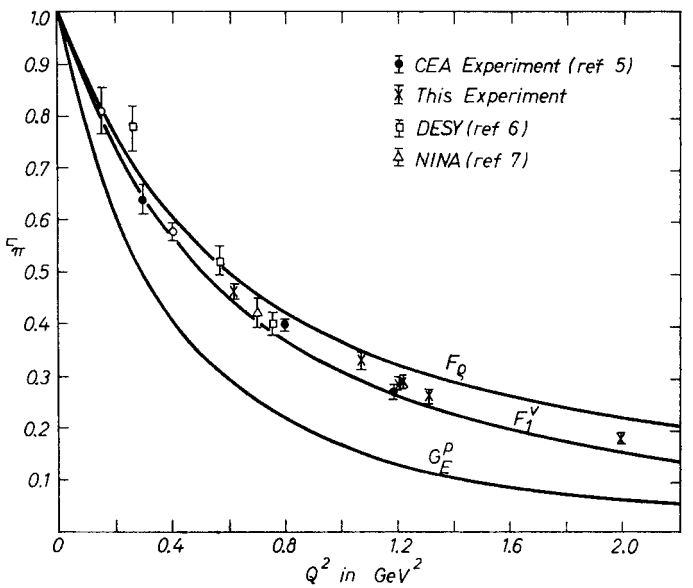

Fig. 15. Results for the pion form factor as extracted from π^+n electroproduction experiments [8, 10, 11]

we can extract $F_\pi(Q^2)$ from the electroproduction data (Fig. 15). The model is certainly not entirely correct for the large production angles, and the longitudinal-transverse interference term, although small, has the wrong sign. However, in the forward direction the model represents the data rather well; it correctly reproduces the Q^2 dependence: an increase followed by a slow decrease (Fig. 14). Form factor determinations made at fixed Q^2 but different W (Fig. 15) are completely consistent, even though the cross section varies rapidly with W. The uncertainty in F_π coming from uncertainties in the model is minimized

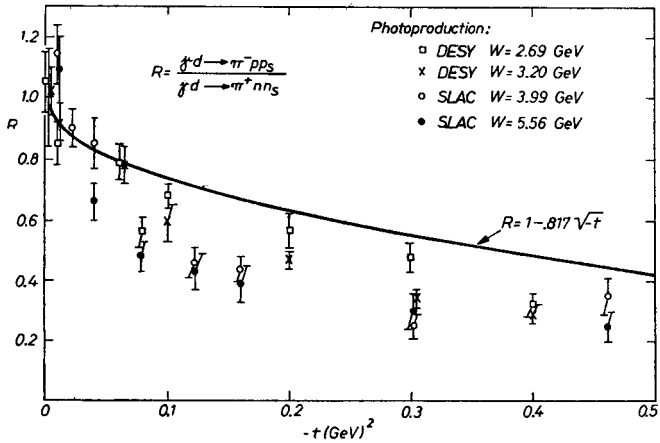

Fig. 16. Comparison of electroproduction (curve [5]) and photoproduction measurements of the ratio of π^-p and π^+n produced from deuterium

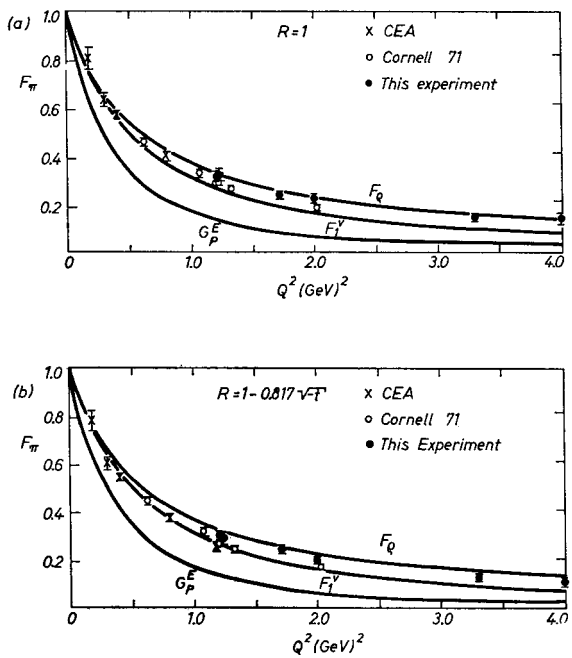

Fig. 17. Pion form factor determinations using π^+n electroproduction data alone [5, 8] (top), and using the isovector electroproduction data [5, 8] (bottom)

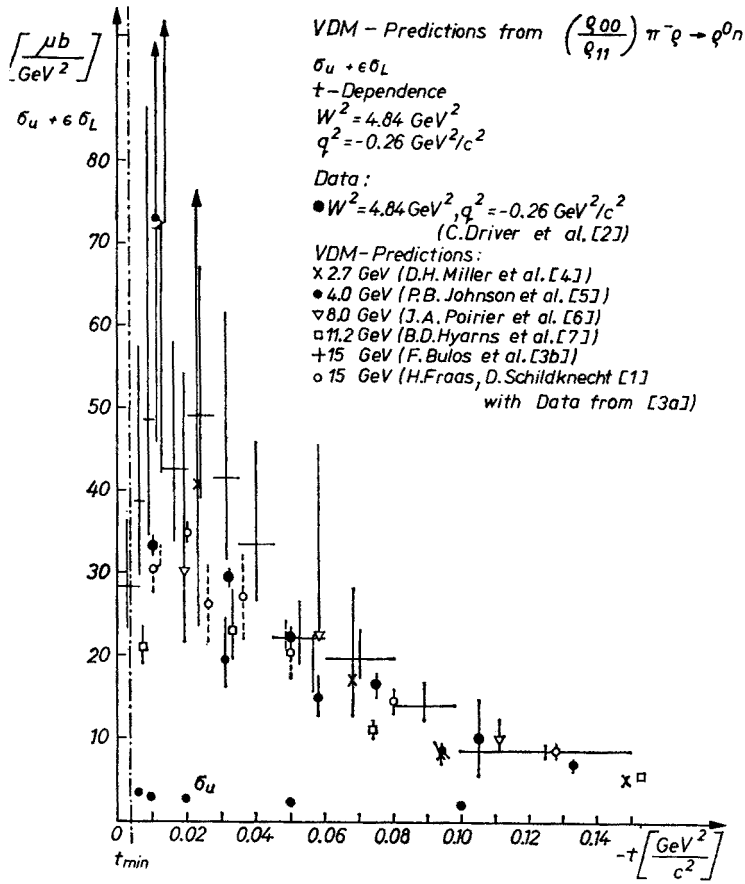

Fig. 18. Comparison of DESY [10] $\pi^+ n$ electroproduction data with a vector dominance prediction [19]

at high W and forward angles where the pion pole is very close to the physical region, and the cross section is therefore essentially proportional to F_π^2. The most recent data from the Harvard group at Cornell [5] extend the measurements up to $Q^2 = 4\ \mathrm{GeV}^2$. They have improved the reliability of the analysis by measuring the π^+/π^- ratio from deuterium, thereby determining the isovector cross section (Fig. 16). Since the standard dispersion theory [18] assumes that the process is pure isovector, the measured isovector part should give a better determination of F_π. Actually, it makes only a slight difference (Fig. 17) in the result.

As one can see from the data (Figs 15 and 17) $F_\pi(Q^2)$ is not far from the most naive ϱ-pole form,

$$F_\pi \approx \frac{m_\varrho^2}{m_\varrho^2 + Q^2},$$

which is completely inconsistent with the nucleon form factor data. It takes very little modification of the simple ϱ-pole, taking account of finite width, the ϱ', or continuum,

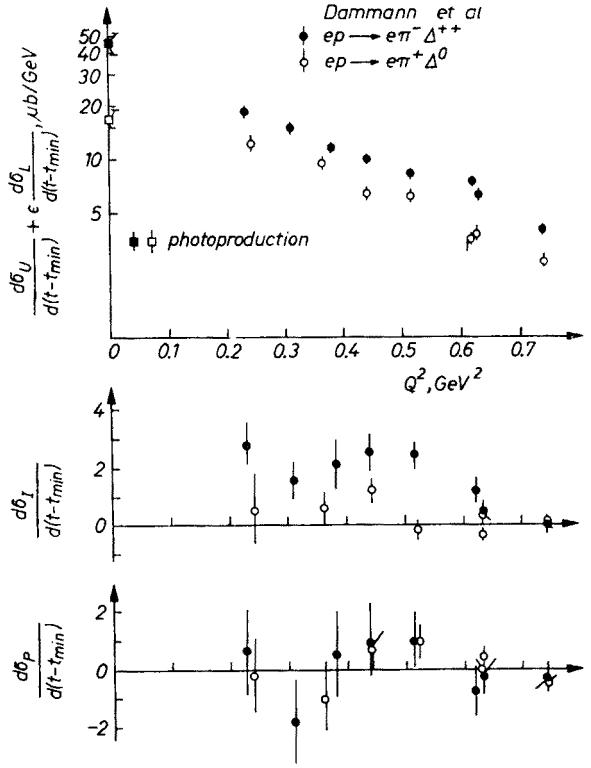

Fig. 19. DESY data [10] on $\pi\Delta$ electroproduction

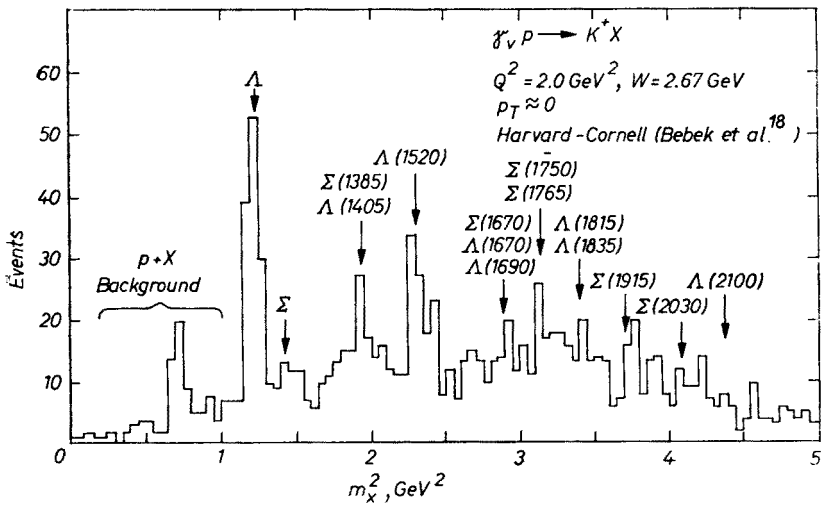

Fig. 20. A typical missing mass spectrum [8] obtained from e, K^+ coincidence data

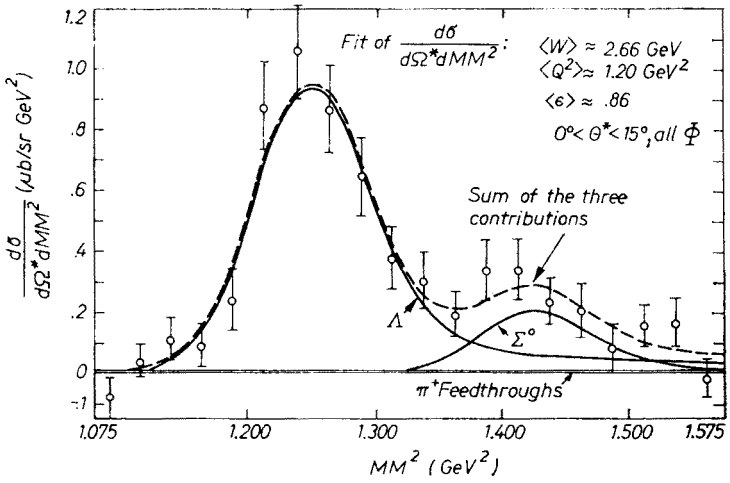

Fig. 21. An e, K^+ missing mass spectrum [8] showing fits to the $K^+\Lambda$ and $K^+\Sigma^0$ electroproduction contributions

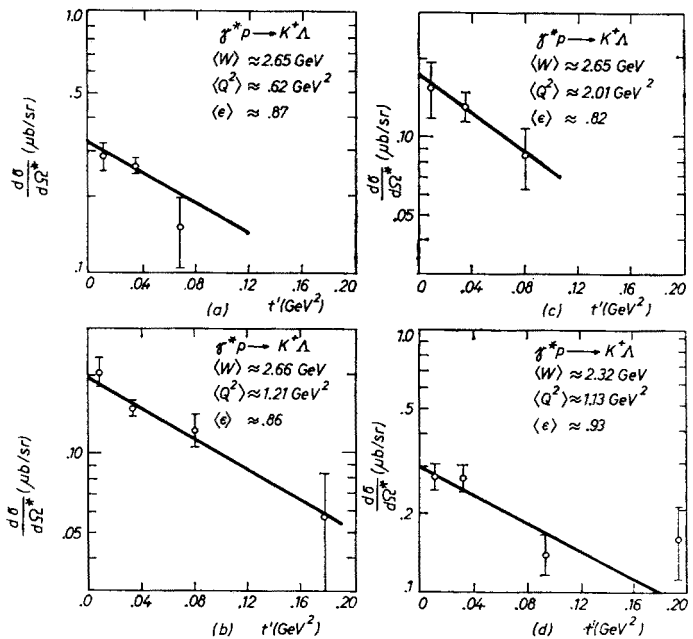

Fig. 22. Harvard-Cornell data [8] on the t dependence of $K^+\Lambda$ electroproduction

to fit the data arbitrarily well. Of course, if the electric Born model is nonsense, then everything I say about F_π is nonsense, too.

We can ask whether the data on $\gamma_V p \to \pi^+ n$ are consistent with vector meson dominance (plus charge symmetry) and the data on the "reversed" reaction $\pi^- p \to \varrho^0 n$. We already know that the test fails when applied to ordinary (transverse) photoproduction data.

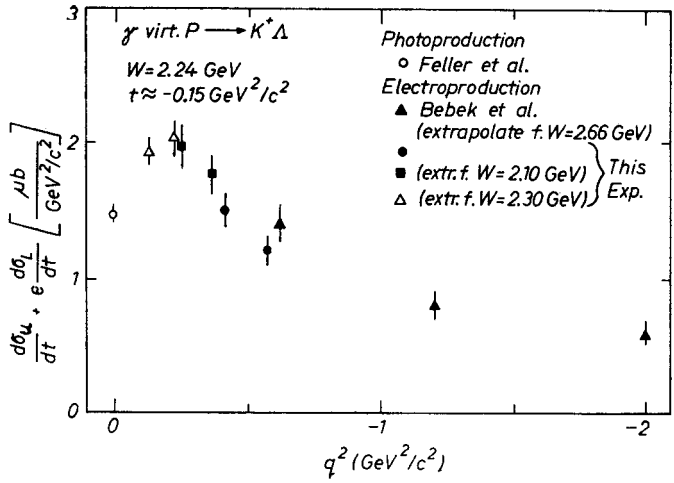

Fig. 23. Harvard-Cornell [8] and DESY [10] data on the Q^2 dependence of $K^+\Lambda$ electroproduction

So what has been done [19] is to compare the electroproduction data (which is predominantly longitudinal) with a "vector dominance prediction" in which only the relative strength of the longitudinal contribution is taken from the experimental ratio $\varrho_{00}/\varrho_{11}$ of density matrix elements in ϱ^0 production by pions, and the rest is just taken from photo-

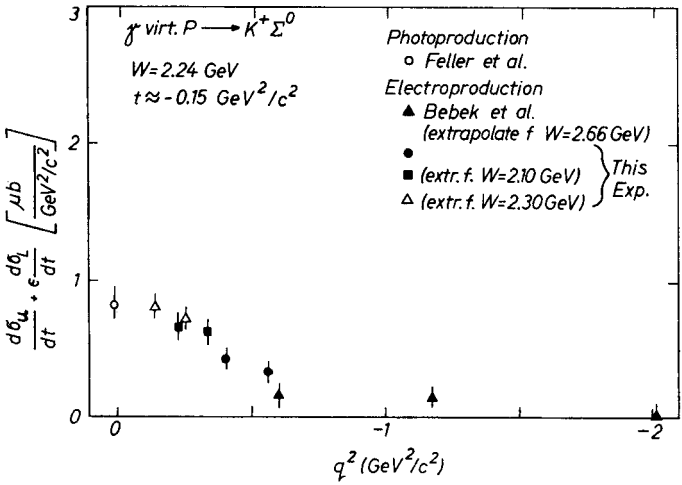

Fig. 24. Harvard-Cornell [8] and DESY [10] data on the Q^2 dependence of $K^+\Sigma^0$ electroproduction

production. The most naive ϱ-pole assumption, along with the threshold Q^2 factor in $d\sigma_L/dt$, are taken for the Q^2 dependence (Fig. 18). The fact that one obtains qualitative agreement is probably not very significant as a test of vector meson dominance, but it does give independent support to the claim that the electroproduction cross section is predominantly longitudinal.

Independently of any models, however, it is an experimental fact (Figs 13 and 14) that the $\gamma_V p \to \pi^+ n$ production cross section actually increases with Q^2 and then drops off rather slowly. This is true whether or not one wants to attribute the effect to the longitudinal contribution and the one-pion-exchange graph. Actually, there is an experiment in progress now, by the Harvard group at the Cornell synchrotron, in which the longitudinal and transverse separation is being attempted. Preliminary indications are that the longitudinal contribution to the $\pi^+ n$ channel is indeed large.

What about the other non-diffractive channels? One would expect that the angular momentum conservation argument, which predicts a large longitudinal contribution to the single-meson-exchange amplitude, would work for any pseudoscalar meson plus baryon channel: $\pi^\pm \Delta$, $K^+ Y^0$ and so on. Indeed the data on $\pi^+ \Delta^0$ and $\pi^- \Delta^{++}$ (Fig. 19) show the same slow decrease with Q^2 that we saw in the $\pi^+ n$ channel.

Fig. 20 shows an experimental missing mass spectrum obtained from e, K^+ coincidences. Evidence is clearly seen for production of $K^+\Lambda$, $K^+\Lambda^*$ (1405) and $K^+\Sigma^*$ (1385) combined, $K^+\Lambda^*$ (1520), and perhaps others. Again, one extracts cross sections by fitting these peaks (Fig. 21). The $K^+\Lambda$ cross section is measured rather well (Fig. 22), but the $K^+\Sigma^0$ is very much smaller, although the two are not very different in photoproduction. This phenomenon can be seen more clearly in the Q^2 dependences (Figs 23 and 24): the early rise in the $K^+\Lambda$ cross section is absent in the $K^+\Sigma^0$ channel. This can be explained by the fact that the ratio of the single-kaon exchange amplitudes for the two reactions is proportional to the ratio of couplings $g_{K\Lambda N}/g_{K\Sigma N}$ which is known to be large.

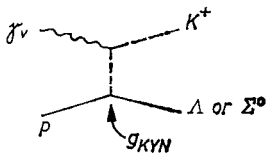

In summary, it is clear that the non-diffractive channels $\pi^+ n$, $\pi^+\Delta$, $K^+\Lambda$ etc. represent a larger fraction of the total $\gamma_V p$ cross section at $Q^2 = 1$ GeV^2 than in photoproduction.

3. Diffractive two-body channels

Rho, omega, and phi production have been measured in experiments of type (b), (c) and (e) (see section A-3, above). In the type (b) experiments the vector mesons are seen as bumps in the $e+p$ missing mass spectrum (Fig. 25); in the other experiments

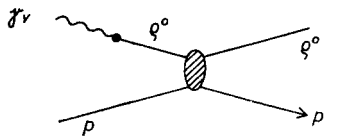

the decay products are seen directly (Fig. 26). The most extensive data concern ϱ^0 production. The total cross section for $\gamma_V p \to \varrho^0 p$ is rather flat in W, as it is in photoproduction, but it decreases rapidly with increasing Q^2 (Fig. 27). The falloff is qualitatively consistent with the square of a rho propagator $m_\varrho^4/(Q^2+m_\varrho^2)^2$, as one would expect from the most naive

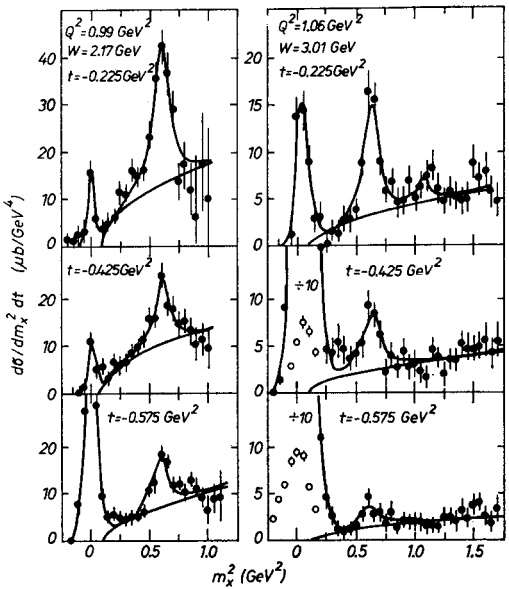

Fig. 25. Typical e, p missing mass spectra obtained in a Cornell experiment [13]. The peaks at 0, 0.6, and 1.1 GeV^2 are the γ, ϱ^0 (and ω), and φ, respectively

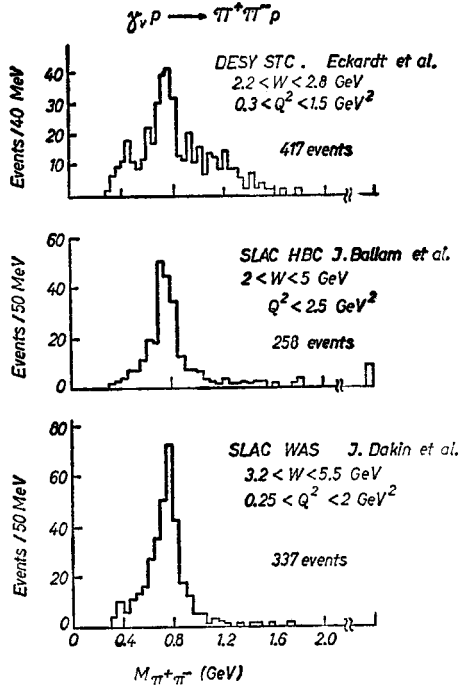

Fig. 26. Mass distribution of $\pi^+\pi^-$ pairs electroproduced in large-aperture experiments [15–17]

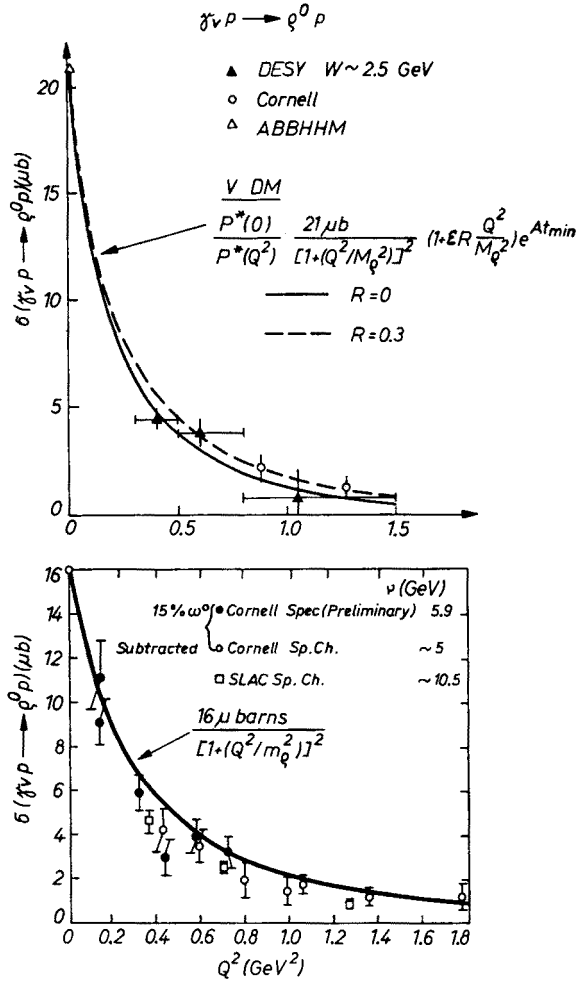

Fig. 27. Measurements [13–15, 17] of the cross section for $\gamma_V p \rightarrow \varrho^0 p$ plotted against Q^2 (for two ranges of W) and compared with vector dominance predictions

rho-dominance model. There should also be a slight Q^2 dependence coming from the variation in the minimum $|t|$ value:

$$|t_{\min}| \approx \left(\frac{Q^2+m_\varrho^2}{2\nu}\right)^2.$$

This rapid decrease in the rho cross section contrasts with the behavior of the non-diffractive channels and suggests that there is very little longitudinal contribution to diffractive production.

The t distributions (Fig. 28) have the same diffractive appearance as in photoproduction (Fig. 10); however there is a systematic flattening of the slope with increasing values

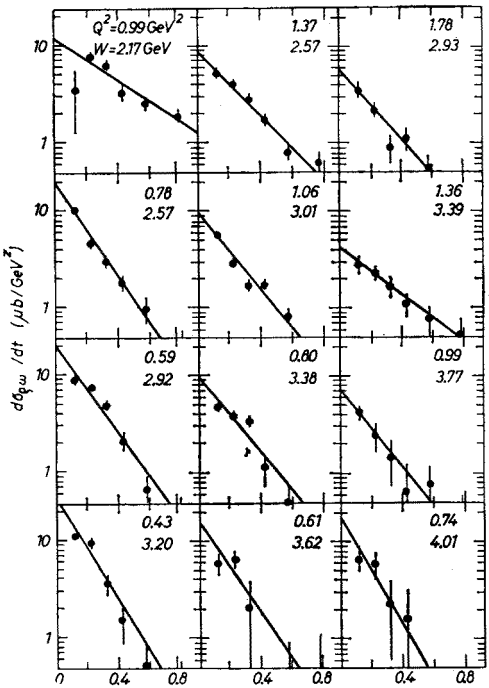

Fig. 28. Cornell measurements [13] of $-t$ (GeV^2) distributions in ϱ^0 and ω electroproduction

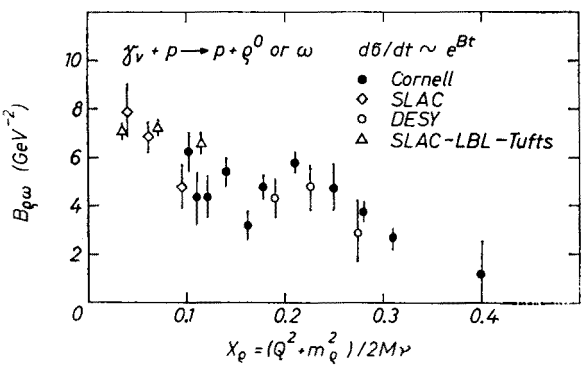

Fig. 29. Dependence of the measured slopes [13, 15, 17] of the t distribution in $\gamma_V p \rightarrow \varrho^0 p$ or ωp on the variable $x_\varrho = (Q^2+m_\varrho^2)/2M\nu$

of the ratio $x_\varrho = \dfrac{Q^2+m_\varrho^2}{2M\nu}$ (Fig. 29). A number of models have predicted this kind of behavior.

The ϱ decay angular distribution has been measured (Fig. 30). Since one cannot easily vary the admixture of helicity components in the virtual photon beam, it is not possible yet to make an unambiguous test of s-channel helicity conservation, as in photo-

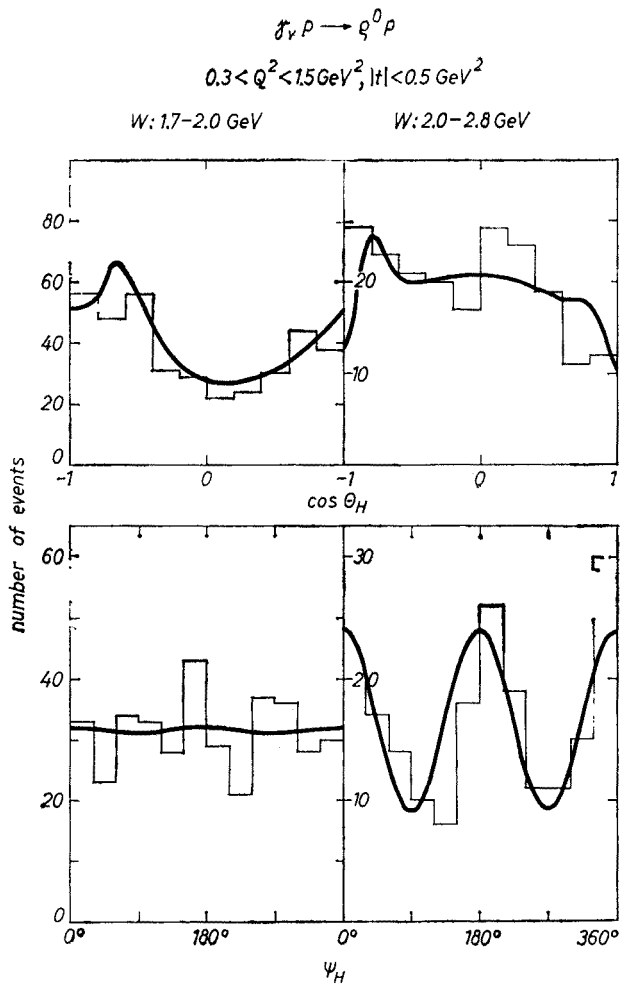

Fig. 30. Polar and azimuthal angle distributions in electroproduced ϱ^0 decays, measured at DESY [17]

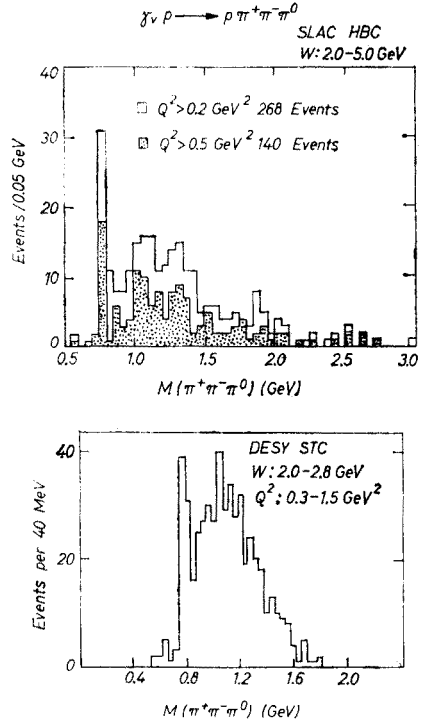

Fig. 31. Mass distributions for $\pi^+\pi^-\pi^0$ observed in electroproduction experiments [16, 17]

production. However, all density matrix elements proportional to helicity flip amplitudes are consistent with zero, so that it is tempting to assume that s-channel helicity is conserved in electroproduction. We can then use the zero-helicity rhos in the final state to measure $\sigma_L(\gamma_V p \to \varrho^0 p)$. The result [15, 17] is that at $Q^2 \approx m_\varrho^2$ we have $\sigma_L \approx 0.5\,\sigma_T$, a much smaller longitudinal effect than in pseudoscalar meson electroproduction.

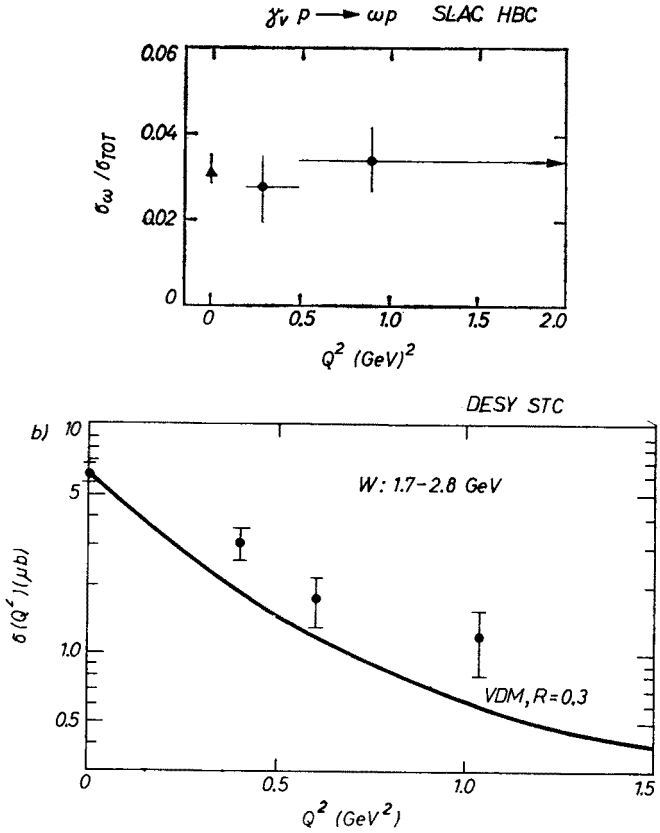

Fig. 32. Q^2 dependence of ω electroproduction [16, 17]

It is clear from Fig. 27 that ϱ^0 production accounts for a decreasing fraction of the total $\gamma_V p$ cross section as Q^2 increases. The rather meager data on φ production [13, 15] are consistent with the same conclusion. The ω data (Figs 31 and 32) do not seem to show as rapid a decrease, but since there is good evidence from photoproduction for a considerable non-diffractive contribution to ω production, this is not so surprising.

Summarizing what we have learned about the two-body channels in the low-Q^2 region, we have

(a) the ratio of non-diffractive/diffractive cross sections increases as Q^2 increases;

(b) the longitudinal contribution increases, and is associated mainly with PS-meson exchange processes (thus $\sigma(K^+\Lambda) \gg \sigma(K^+\Sigma^0)$);

(c) the width of the forward peak in vector meson production increases.

4. Inclusive reactions

The longitudinal momentum distributions for $\gamma_V + p \to \pi^+ + \text{anything}$ (Figs 33, 34, 35) are like those observed in ordinary photoproduction except for the absence of the forward-hemisphere plateau coming from rho production and decay. The flattening of the transverse momentum distributions (Fig. 36) with increasing Q^2 can also be understood in terms of the disappearance of the diffractive channels (and also the vector meson t distributions). On the other hand, the p_T distribution in the central region (Fig. 37) seems to be independent of Q^2. The data on p_T^2 slopes are summarized in Fig. 38.

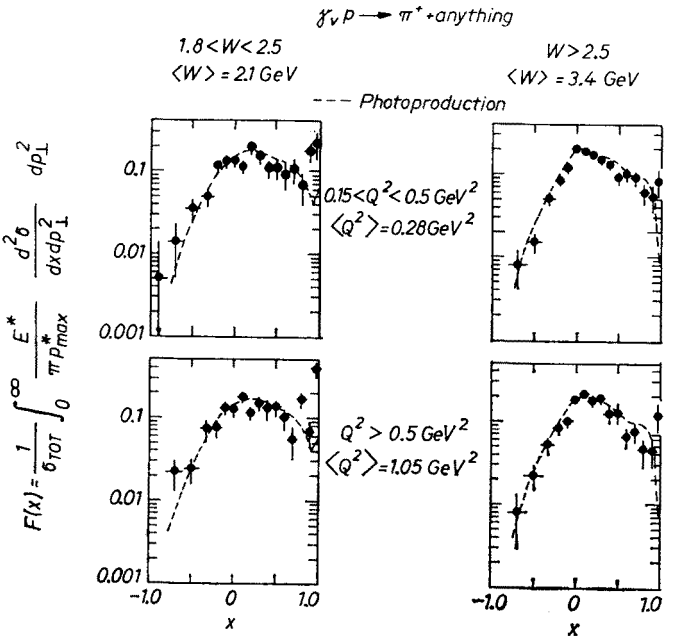

Fig. 33. SLAC data [16] on the invariant inclusive cross section for $\gamma_V + p \to \pi^+ +$ anything, integrated over transverse momentum p_T and plotted against longitudinal momentum $x = p_L/p_{max}$

Fig. 39 shows an example of the longitudinal momentum distribution for protons from $\gamma_V + p \to p +$ anything, illustrating that (a) protons are emitted mainly in the backward hemisphere, and (b) there is no Q^2 dependence in the forward proton production. As we expect, the leading particle peak at $x = p_L/p_{max} < -0.8$, corresponding to vector meson production, decreases rapidly with increasing Q^2. The average level of $(1/\sigma)(d\sigma/dx)$ in the backward hemisphere is a measure of $\bar{n}_p$, the average probability per event of having a proton (rather than a neutron) in the final state. That is,

$$\bar{n}_p = \frac{1}{\sigma} \int_{-1}^{1} \frac{d\sigma}{dx} dx \approx \frac{1}{\sigma} \int_{-1}^{0} \frac{d\sigma}{dx} dx \approx \frac{1}{\sigma} \left\langle \frac{d\sigma}{dx} \right\rangle .$$

This quantity is plotted against Q^2 in Fig. 40. Note that as Q^2 increases $\bar{n}_p$ decreases from about 0.7, its photoproduction value [3], to less than 0.5. This is presumably caused

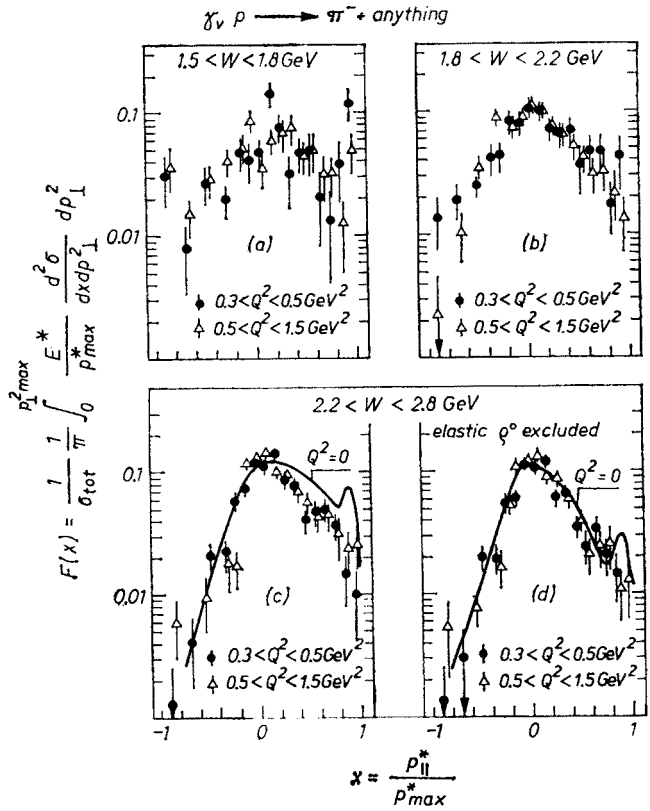

Fig. 34. DESY data [17] on $\gamma_V + p \to \pi^- +$anything, integrated over p_T and plotted against $x \approx p_L/p_{max}$

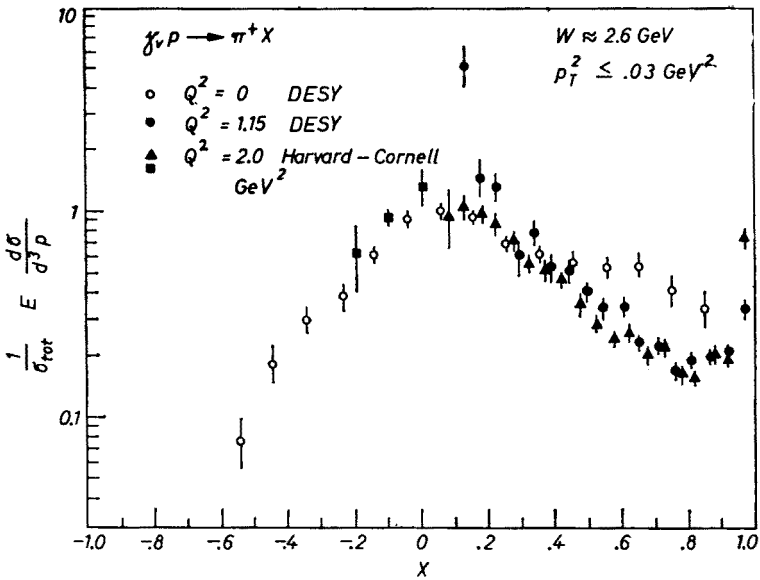

Fig. 35. Harvard-Cornell [8] and DESY [9] data on $\gamma_V + p \to \pi^+ +$ anything, plotted against $x = p_L/p_{max}$, for $p_T \approx 0$

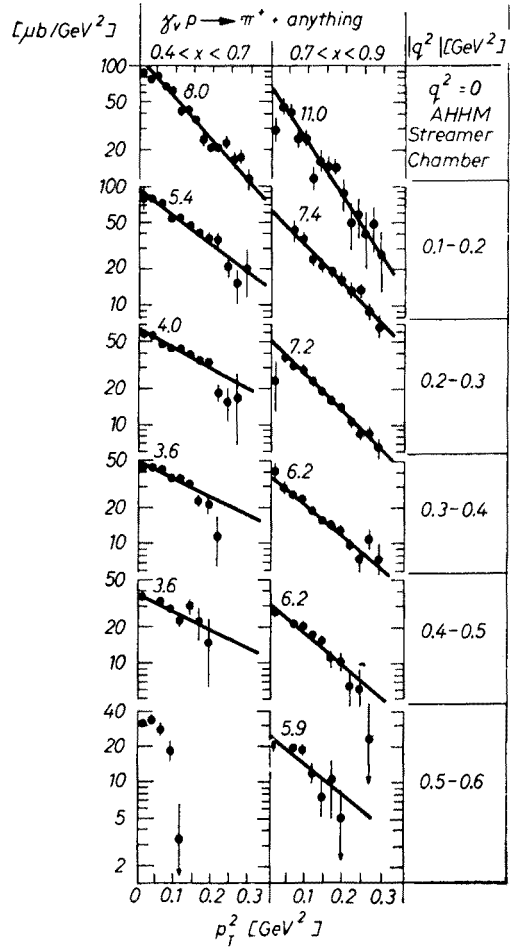

Fig. 36. DESY data [10] on the p_T dependence of the inclusive cross section for π^+ electroproduction, for forward pions ($x > 0.4$)

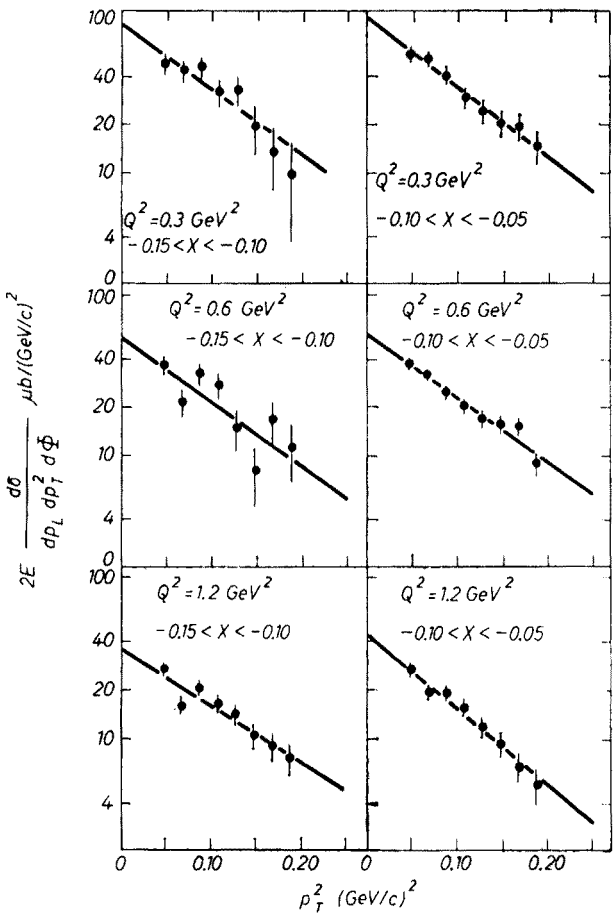

Fig. 37. Cornell data [13] on the p_T dependence of the inclusive cross section for π^+ electroproduction, for central values of longitudinal momentum ($x < 0$)

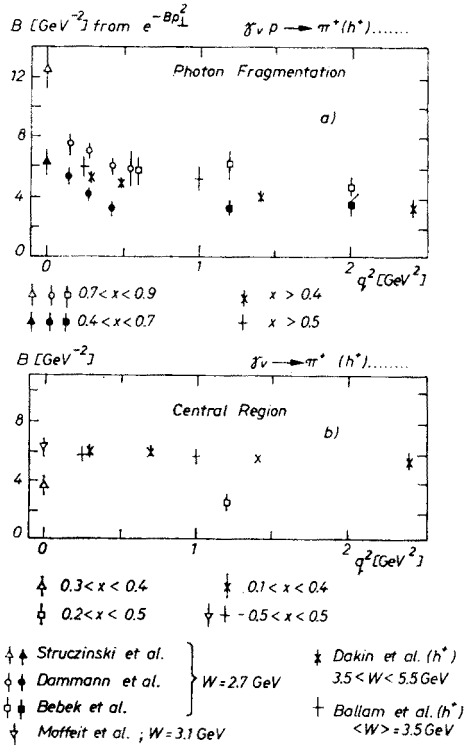

Fig. 38. A summary [1] of slopes of pion transverse momentum distributions measured in electroproduction

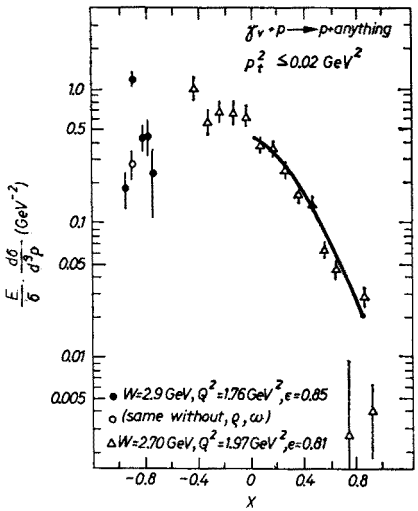

Fig. 39. A typical inclusive spectrum [8, 13] of longitudinal proton momenta observed in electroproduction, compared with photoproduction at the same W (curve)

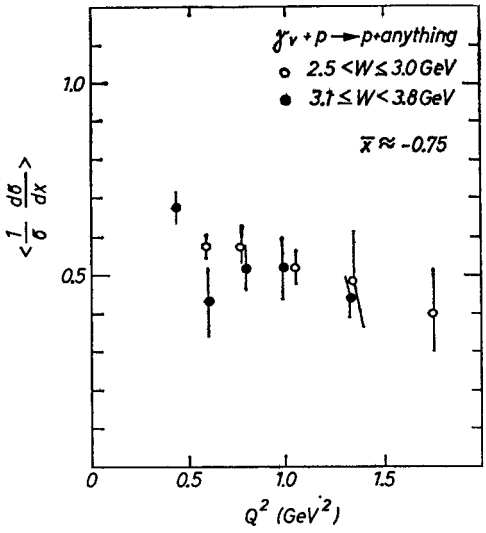

Fig. 40. Q^2 dependence [13] of the average $(1/\sigma)$ $(d\sigma/dx)$. This is approximately $\bar{n}_p$, the average proton multiplicity. In photoproduction $\bar{n}_p$ is estimated [3] to be about 0.7

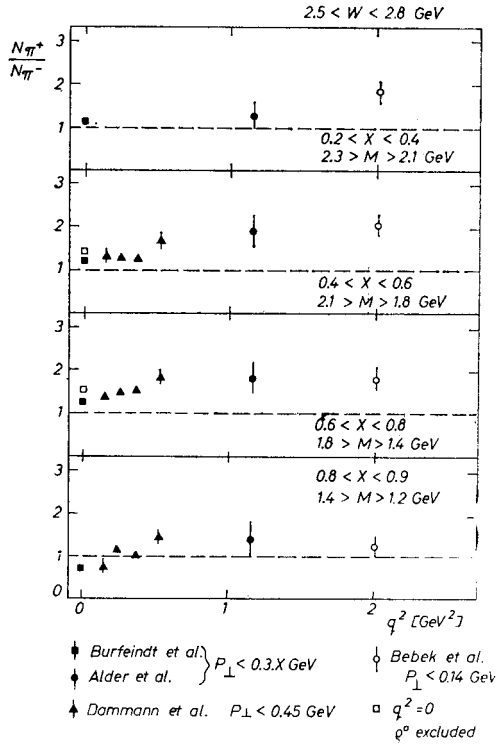

Fig. 41. A summary [1] of measurements of π^+/π^- for pions electroproduced at $x = p_L/p_{max} > 0.2$

by the decrease in diffractive channels (which always have a proton in the final state) and the increasing contribution of processes in which the positive charge of the initial $\gamma_V p$ state is carried forward in the final state by a single meson.

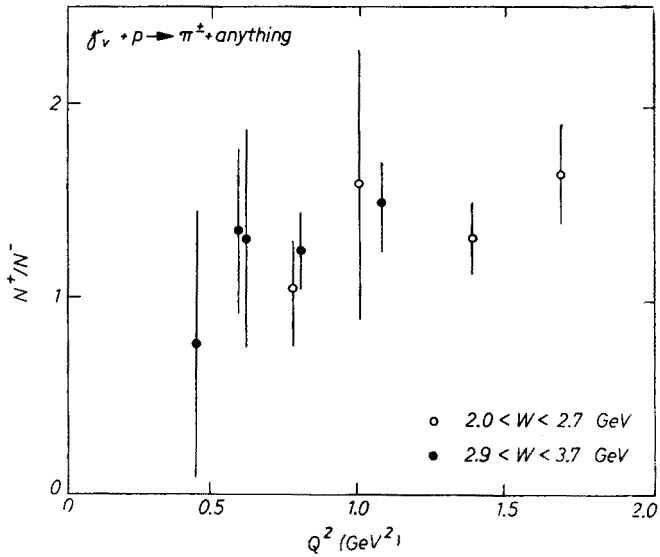

Fig. 42. Cornell data [13] on π^+/π^- for pions electroproduced backward ($x < 0.2$)

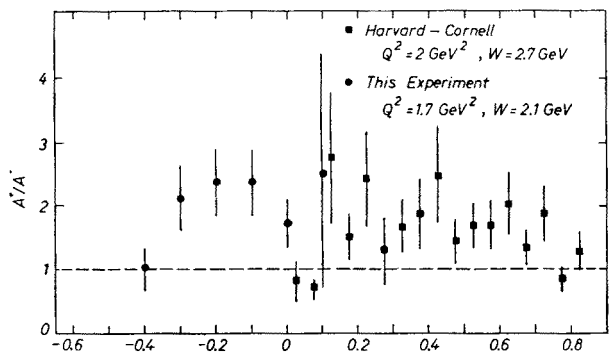

Fig 43. Harvard [8] and Cornell [13] data on the dependence of π^+/π^- on fractional longitudinal momentum

The effects are of course also manifested in the π^+/π^- production ratio. As the ratio of diffractive production (for which $\pi^+/\pi^- = 1$) to non-diffractive processes (such as π^+n) decreases with increasing Q^2, the π^+/π^- ratio increases from typically 1.2 in photoproduction to almost 2 at $Q^2 \approx 2\ GeV^2$ (Figs 41 and 42). This seems to occur for all values of longitudinal momentum (Fig. 43), although not necessarily uniformly. The ratio does vary significantly with transverse momentum, however (Fig. 44).

The average charged hadron multiplicity decreases somewhat with increasing Q^2 [16, 17] as the diffractive production (usually three-prongs) decreases and the π^+n, etc.

(one-prong) increases. I will show the evidence for this when I discuss the data in the scaling region. It is interesting to note that the data on the average charged hadron multiplicity $\bar{n}$, the average proton multiplicity $\bar{n}_p$ and the pion charge ratio $\bar{n}_+/\bar{n}_-$ (assuming it is uniform over phase space) are compatible with charge conservation. Neglecting strange particle final states, charge conservation requires

$$\frac{\bar{n}_+}{\bar{n}_-} = \frac{\bar{n}-2\bar{n}_p+1}{\bar{n}-1} .$$

In the Table below I list experimental values for $\bar{n}$ [6] and $\bar{n}_p$ [13] and the calculated values for $\bar{n}_+/\bar{n}_-$. These predicted charge ratios match the measurements (Fig. 41) rather well. As Q^2 increases the increase in the π^+/π^- ratio is compensated by the decrease in $\bar{n}_p$ and $\bar{n}$.

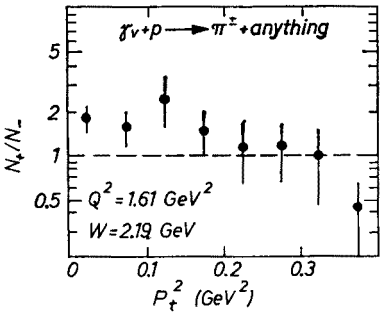

Fig. 44. Cornell data [13] on the dependence of π^+/π^- on transverse momentum

We conclude, therefore, that the low-Q^2 behavior of the inclusive distributions is explainable in terms of the known behavior of the exclusive two-body channels, at least in the W range (<4 GeV) measured so far. This may at first seem rather surprising, since the two-body channels we have looked at account for less than a third of the $\gamma_V p$ cross

TABLE I

Measured charged hadron and proton multiplicities for several Q^2 and W values, with overall π^+/π^- yield ratios calculated from the multiplicities (see text for formulae)

Q^2 (GeV²)	W GeV	$\bar{n}$	$\bar{n}_p$	π^+/π^-
0	3.1	3.07±0.10	0.1 ±0.1	1.29±0.10
1.4	2.9	2.77±0.08	0.44±0.06	1.65±0.12
2.4	3.1	2.89±0.05	0.3 ±0.1	1.74±0.12

section. Perhaps the remainder of the cross section is mainly quasi-two-body and behaves (diffractively or non-diffractively) much like the part we have measured. It will be interesting to see whether this is still true at much higher W, where the simple two-body channels contribute less and less to the cross section.

D. The Scaling Region: $W > 2$ GeV, $Q^2 > 2$ GeV^2

1. Introduction

This is presumably the kinematic region in which to look for evidence of the basic constituents of the proton. Can we see partons or their fragments in the hadronic final states? Unfortunately, this is also the kinematic region which is covered least by the coincidence experiments. Only within the last year or so has it been possible to extend the measurements above $Q^2 = 2$ GeV^2, and only at the Cornell synchrotron are the energy (12 GeV) and beam duty cycle ($\approx 5\%$) sufficient. The data come from two experiments: the Harvard group (Pipkin et al. [5]) measurements of type (a), and the Cornell group (Berkelman et al. [6]) measurements of type (d).

2. The Harvard experiment: inclusive spectra

You recall (Fig. 39) that protons are emitted mainly backward in photoproduction and low-Q^2 electroproduction. Drell, Levy, and Yan [20], however, predicted that as Q^2 increases one should expect to see more and more protons coming out forward. The

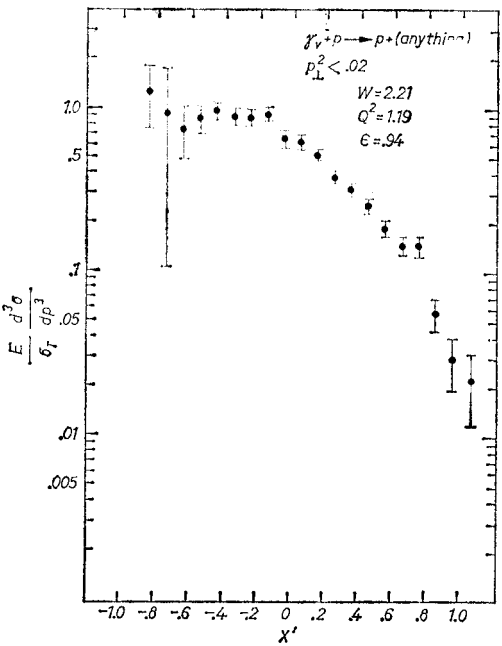

Fig. 45. Invariant cross section for $\gamma_V + p \rightarrow p +$ anything (Harvard [5])

argument is based on the fact that the longitudinal contribution to the single-arm cross section [7] is only 20% or less, and the fact that a transverse photon cannot transfer all its momentum to a spinless parton. Therefore, the partons must have spin, presumably 1/2, and the forward hadron fragments of the parton must contain a fermion, presumably a proton in many cases. The experimental data, however (Figs 45 and 46) show no evidence

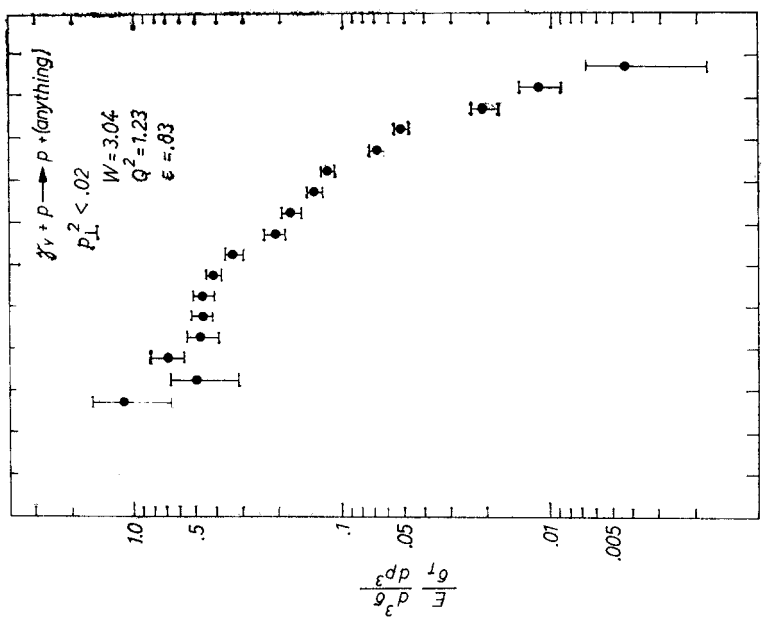

Fig. 47. Invariant cross section for $\gamma v + p \rightarrow p + \text{anything}$ at the same Q^2 as in Fig. 45 but higher W (Harvard [5])

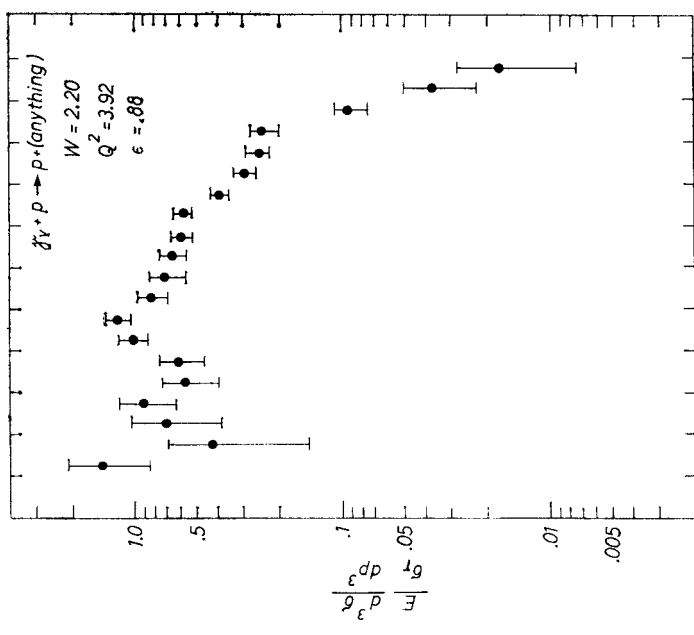

Fig. 46. Invariant cross section for $\gamma v + p \rightarrow p + \text{anything}$ at the same W but higher Q^2 (Harvard [5])

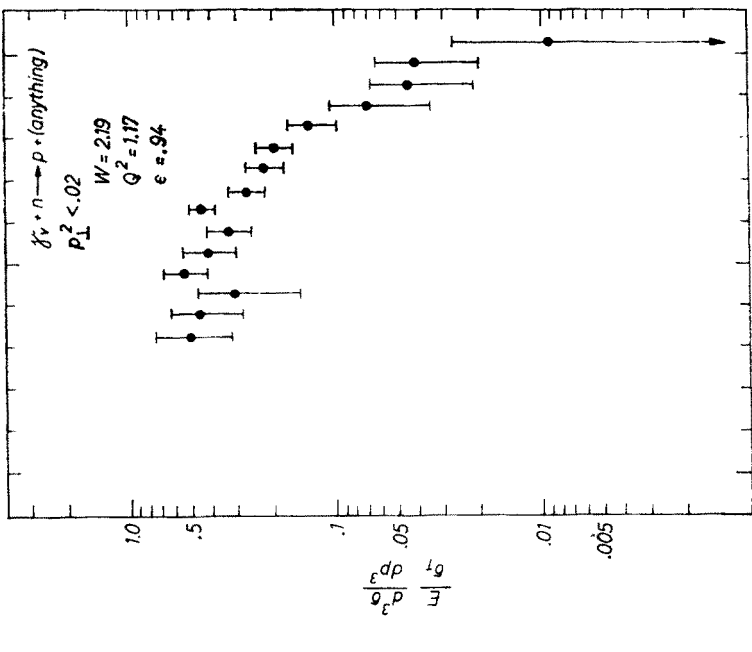

Fig. 49. Invariant cross section for $\gamma\nu + n \rightarrow p +$ anything at the same Q^2 but higher W (Harvard [5])

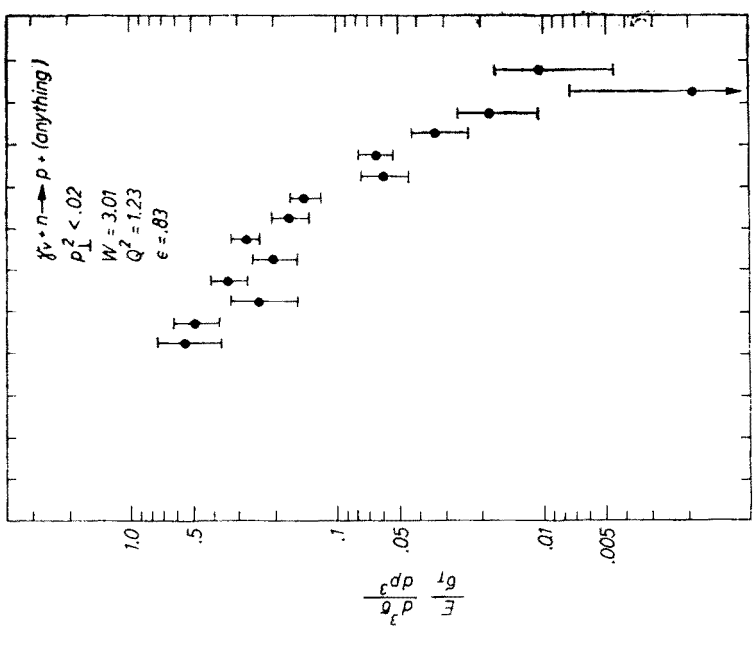

Fig. 48. Invariant cross section for $\gamma\nu + n \rightarrow p +$ anything (Harvard [5])

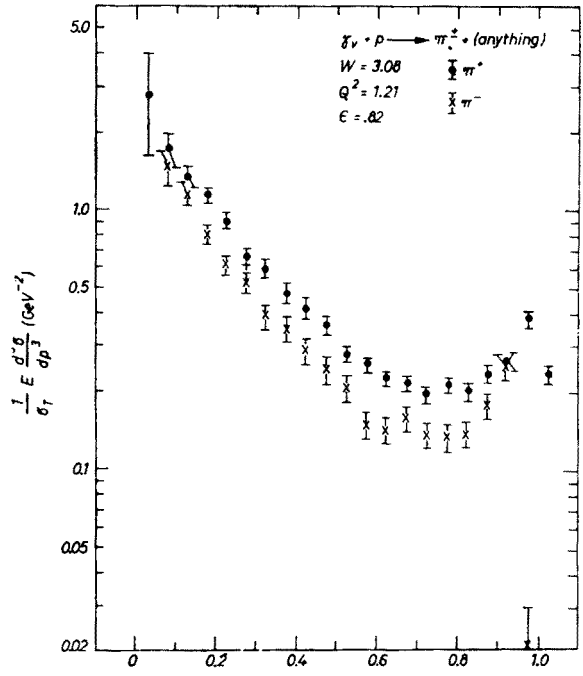

Fig. 50. Harvard data [5] for the inclusive reactions $\gamma_V + p \to \pi^{\pm}$ + anything

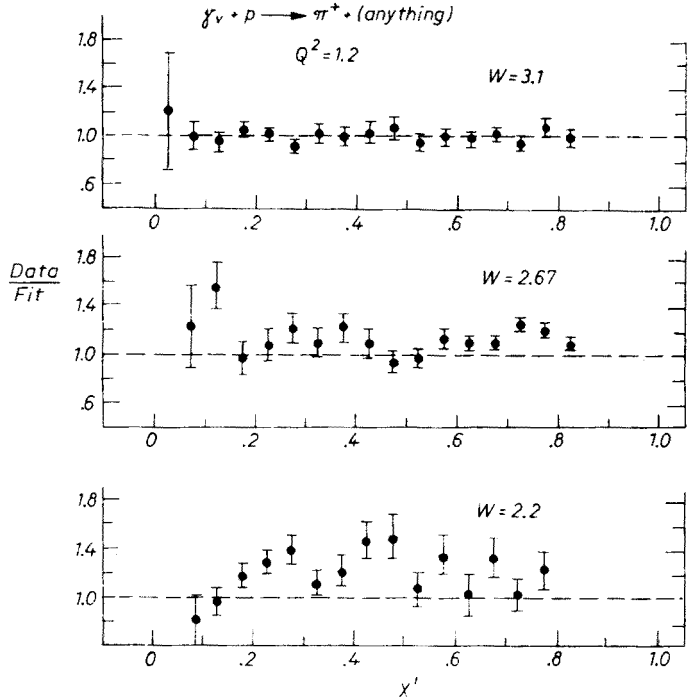

Fig. 51. W dependence at fixed Q^2 for $\gamma_V + p \to \pi^+$ + anything. In each case the invariant cross section has been divided by a polynomial fit to the π^+ data of Fig. 50 (Harvard data [5])

of any Q^2 dependence (at fixed W) in the longitudinal momentum distribution, up to $Q^2 \approx 4$ GeV^2 ($\omega' = 2.2$). There is, however, a W dependence at fixed Q^2 (Figs 45 and 47), the suppression of forward protons being stronger at higher energies. The same behavior holds in the proton spectra from a neutron target (Figs 48 and 49). Although the absence of forward protons does not kill the parton model, I think it must be scored as a point against partons. The Harvard group is now taking data to extend the test to $Q^2 = 10$ GeV^2.

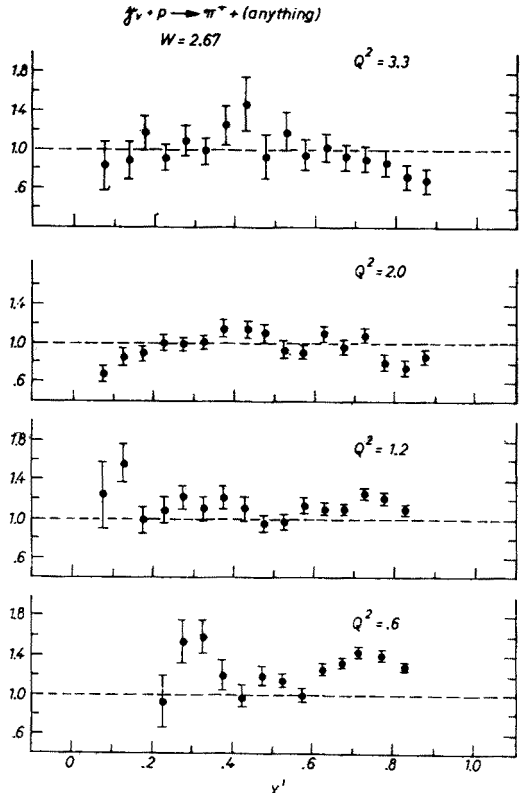

Fig. 52. Q^2 dependence at fixed W for $\gamma_V + p \to \pi^+ +$ anything. In each case the invariant cross section has been divided by a polynomial fit to the π^+ data of Fig. 50 (Harvard data [5])

What about the pion inclusive spectra? In order to make comparisons more easily the π^+ longitudinal spectrum (Fig. 50) at low Q^2 has been fit with a polynomial and the data for other Q^2 and W have been divided by this fit. At fixed Q^2 (Fig. 51) there is some W dependence, but at fixed W (Fig. 52), however, there seems to be little variation with Q^2. Likewise, the π^+/π^- ratio, starting with either a proton (Fig. 50) or neutron (Fig. 53) target, depends mainly on W and not on Q^2 (Fig. 54).

In short, at fixed W nothing seems to change in the inclusive distributions between $Q^2 = 1$ and 4 GeV^2. This makes it rather unlikely that the π^+/π^- ratios have much to do with the charges of the quark partons, although there are those who claim otherwise. Various kinds of scaling in the hadron momentum variables have been proposed for

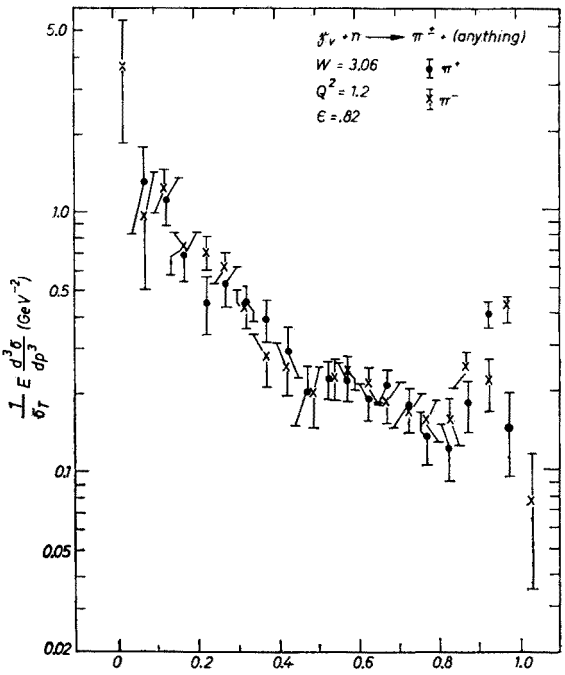

Fig. 53. Harvard data [5] for the inclusive reactions $\gamma_V + n \rightarrow \pi^{\pm} +$ anything

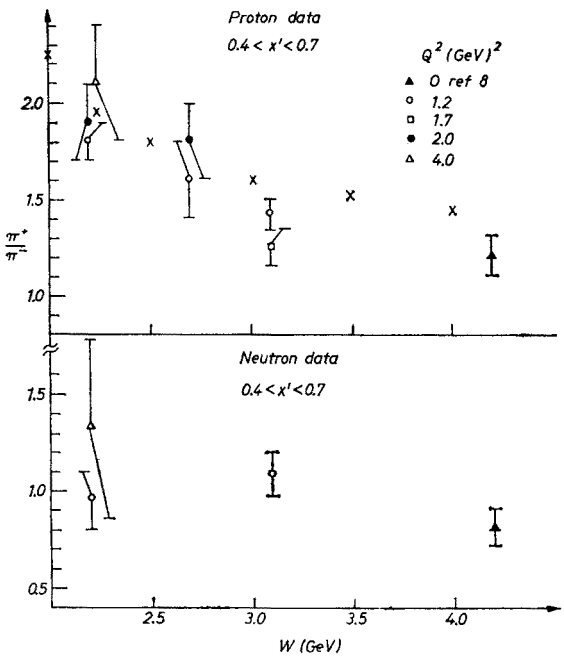

Fig. 54. Q^2 and W dependence of π^+/π^- in $\gamma_V + p \rightarrow \pi^{\pm} +$ anything and in $\gamma_V + n \rightarrow \pi^{\pm} +$ anything (Harvard data [5])

asymptotic values of the momenta. Present energies (up to $W = 4$ GeV) are not sufficient for a serious test of such predictions. The prediction of combined Feynman and Bjorken scaling,

$$\frac{E}{\sigma_V}\frac{d\sigma_V}{d^3p} = f(x_L, p_T, \omega),$$

is certainly violated by the results on $\gamma_V + p \to \pi^\pm$ + anything and $\gamma_V + p \to p$ + anything. A better summary of the data would be

$$\frac{E}{\sigma_V}\frac{d\sigma_V}{d^3p} = f(x_L, p_T, W), \text{ independent of } Q^2.$$

3. The Cornell experiment: multiplicities, etc.

The other experiment [6] at high Q^2 is a measurement of charged hadron multiplicities in electroproduction from proton and neutron targets. A hodoscope array of scintillation counters, almost completely surrounding the target, detected charged hadrons in coinci-

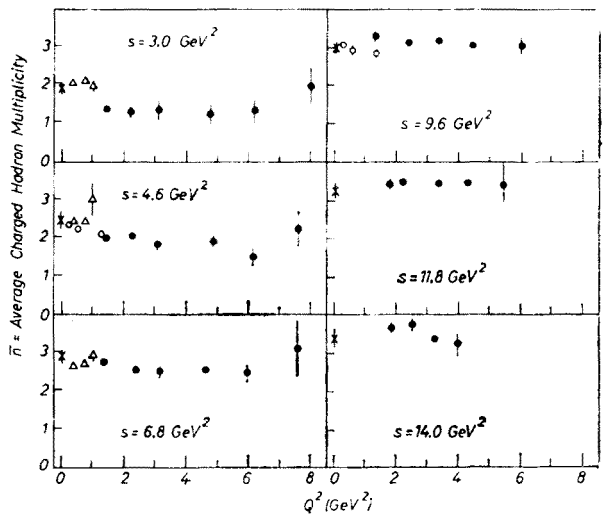

Fig. 55. Average charged hadron multiplicity in $e + p \to e$ + hadrons, plotted against Q^2 for several ranges of $s = W^2$. Data are from DESY [17] (triangles), SLAC [16] (open circles), and Cornell [6] (black circles)

dence with the electron, detected in a magnetic spectrometer. With this technique we observe the average charged multiplicity, the fraction of final states in each multiplicity category, and rough laboratory angular distributions, all as functions of Q^2 and W. Hadrons are not identified, however, and momenta are not measured. This is the price one pays for being able to carry the measurements up to $Q^2 = 8$ GeV^2.

The average ep multiplicity (Fig. 55) at low fixed $W (= \sqrt{s})$ shows a slight decrease between photoproduction and $Q^2 = 1$ GeV^2 (as discussed above in section C–4). Otherwise, it is independent of Q^2 up to about 8 GeV^2. The prong distributions (Fig. 56) show

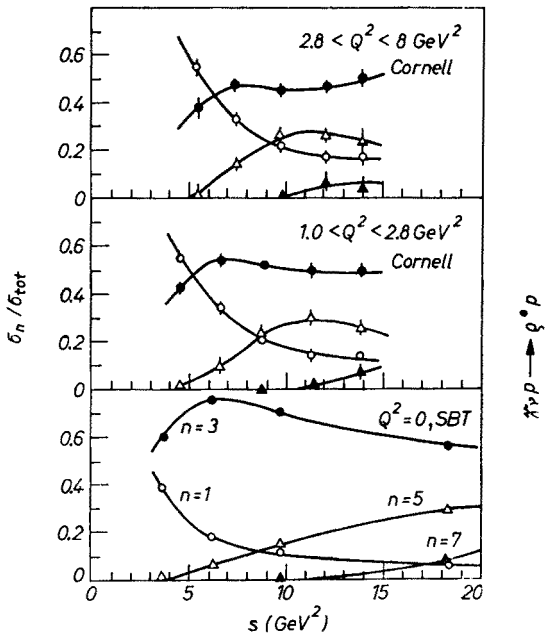

Fig. 56. Measurements of the fractional cross section for n charged hadrons in $e+p \rightarrow e +$ hadrons. Electroproduction data are from Cornell [6]

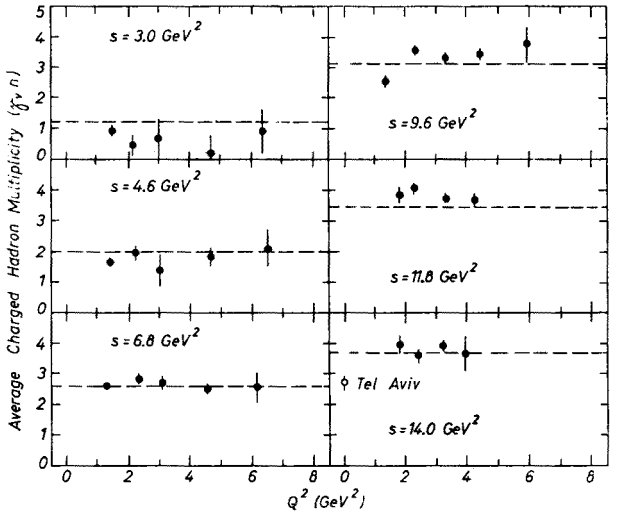

Fig. 57. Average charged hadron multiplicity in $e+n \rightarrow e +$ hadrons, plotted against Q^2 for several ranges of $s = W^2$. Data are from Cornell [6]; the dashed line indicates the average trend of the $e + p$ multiplicities

as expected a decrease in the 3-prong fraction and an increase in the 1-prong fraction in the low-Q^2 transition region, but no variation at high Q^2. Similar conclusions hold for the en reaction (Figs 57 and 58). The s dependences ($s = W^2$), averaged over Q^2, are compared with the s dependence of the charged multiplicity in other reactions in Fig. 59.

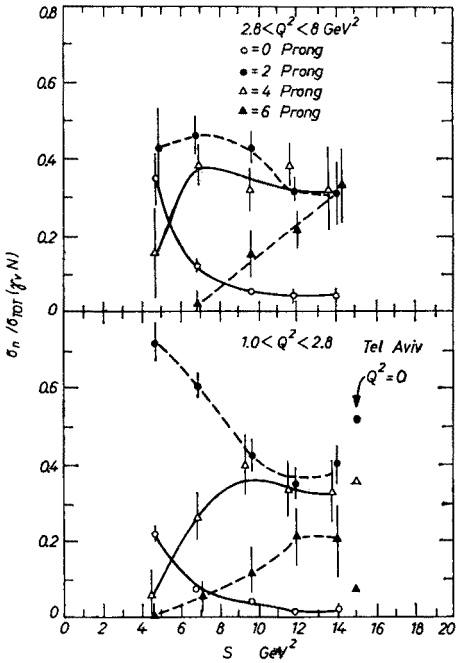

Fig. 58. Measurements from Cornell [6] of the fractional cross section for production of n charged hadrons in $e + n \rightarrow e +$ hadrons

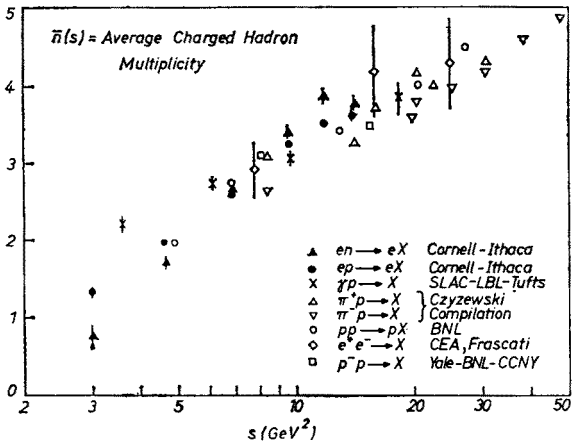

Fig. 59. Measurements of average charged multiplicity compared for several different reactions, as a function of the total effective mass-squared of the hadron final state

I find it remarkable that all of these processes, with cross sections varying over six orders of magnitude, have essentially the same multiplicity. Only at very low s is there any significant dependence on the nature of the particles in the initial state. It is as if the final state were evolved from a state of thermal equilibrium which depends only on the available center of mass energy.

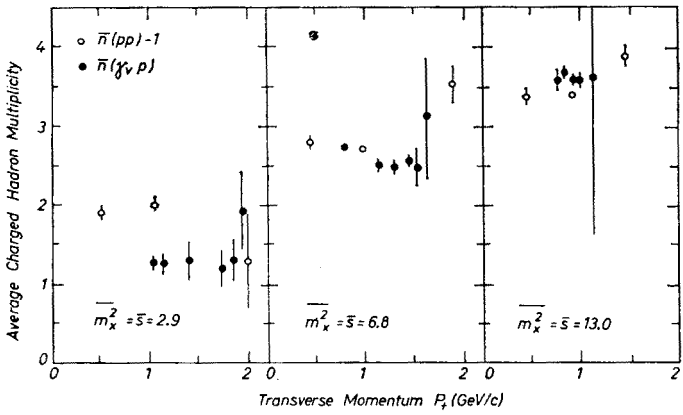

Fig. 60. Comparison of measurements of average charged multiplicity of X in $pp \rightarrow pX$ [21] (open circles) and $ep \rightarrow eX$ [6] as a function of the transverse momentum of the final p or e for several values of the mass of X

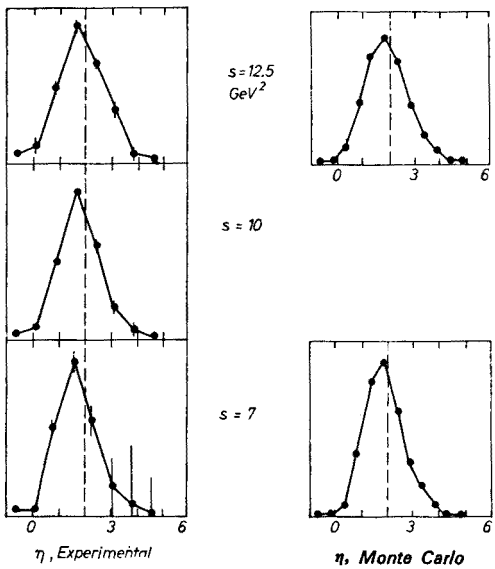

Fig. 61. Cornell measurements [6] of the distribution of hadrons from $e+p \rightarrow e +$ hadrons in laboratory pseudorapidity, $-\ln \tan(\theta/2)$, at fixed Q^2 for several s

One of the experiments included in Fig. 59 is a Brookhaven measurement [21] of the associated multiplicity in $pp \rightarrow pX$. Since their measurements are actually carried out as a function of the transverse momentum of the scattered proton as well as the missing mass m_X, it is rather closely parallel to the $ep \rightarrow eX$ experiment. The comparison as a function of p_T (proton or electron) for various values of $m_X^2 = W^2$ is shown in Fig. 60. The agreement is very good, in spite of the fact that the two processes are, a priori, unrelated. The pp data may suggest an upward trend in the associated multiplicity at high p_T. The electroproduction data neither confirm it nor contradict it.

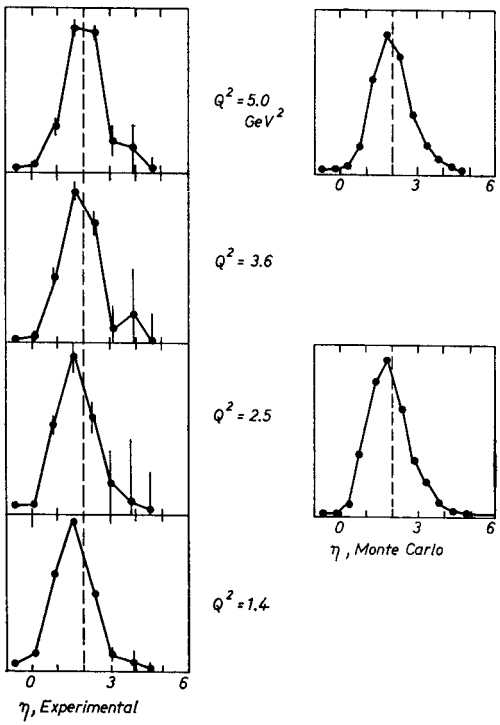

Fig. 62. Cornell measurements [6] of the distribution of hadrons in pseudorapidity, at fixed s for several Q^2

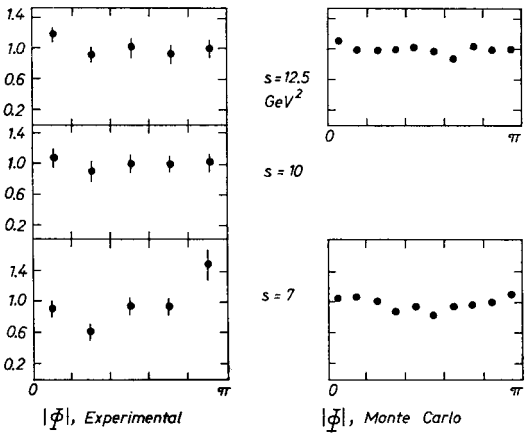

Fig. 63. Cornell measurements [6] of the azimuthal distribution of hadrons in $e+p \rightarrow e +$ hadrons, for fixed Q^2 at several values of s

The laboratory-angle distributions are plotted (Figs 61–64) against pseudorapidity $\eta = -\ln \tan(\theta_{lab}/2)$ and azimuth φ — both with respect to the virtual photon axis. The inclusive pseudorapidity distributions (Figs 61 and 62) show no dynamic effects as a function of either s or Q^2. Both the broadening of the peak with increasing s (Fig. 61)

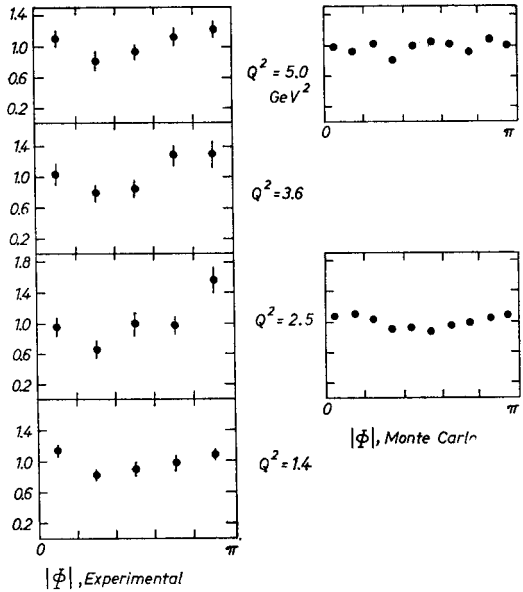

Fig. 64. Cornell data [6] on the azimuthal distribution of hadrons in $e+p \to e +$ hadrons, for fixed s at several values of Q^2

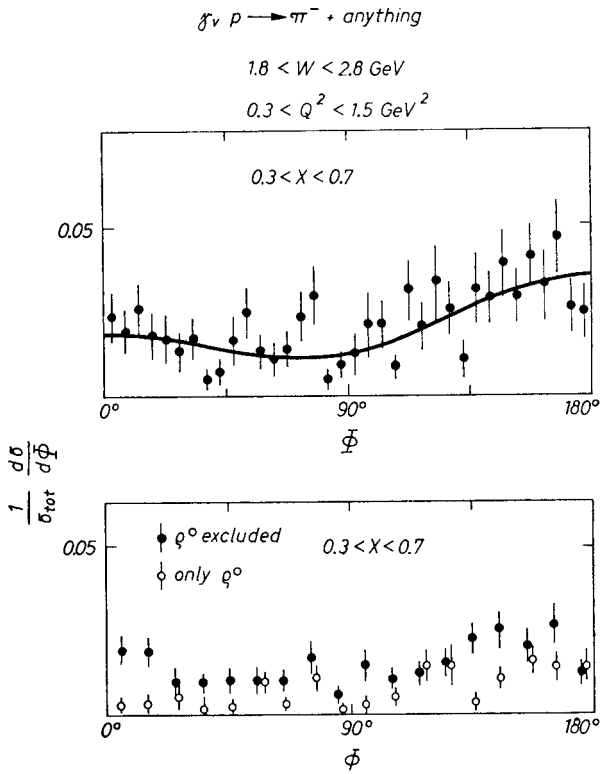

Fig. 65. DESY data [17] on the azimuthal distribution of π^- in $e+p \to e+\pi^-+$ anything

and the slight shift with increasing Q^2 (Fig. 62) are purely kinematic effects, which show up also in a Monte Carlo calculation based on phase space and limited transverse momentum. The φ distributions (Figs 63 and 64) are mainly flat, with a slight tendency toward asymmetry at the lowest s (Fig. 63), but no variation with Q^2 (Fig. 64). The asymmetry is similar to that observed in photoproduction, and which is attributed to the ϱ^0 production channel. It has also been observed in low-Q^2 electroproduction (Fig. 65). Since the asymmetry is slight and confined to low W, our data (Figs 63 and 64) are not in significant disagreement with Ravndal's prediction of no azimuthal asymmetry, based on the parton model.

4. Summary

The easiest way to summarize the results of these two experiments in the scaling region is to say that, outside of the overall Q^2 dependence of the total γ_V+N cross section, *nothing* in the final states has any dependence on Q^2 at fixed W. Note that this seems to be true even at $\omega \approx 2$, where the νW_2 function varies significantly with ω, and the neutron and proton scatter quite differently. For the final states, the scaling variable ω appears to be irrelevant; the only functional dependence is on the center of mass energy W. There is apparently nothing in the final hadron state which depends on the charge or fractional momentum of the struck parton. Again, although this does not kill the parton model, it must surely be scored against it. Perhaps the interaction cross section is determined by the initial virtual-photon-parton collision, but the final states are the result of a thermodynamic process which wipes out any memory of the initial state and gives us the same multiplicities and inclusive distributions we get from any purely hadronic collision at the same energy.

REFERENCES

[1] F. W. Brasse, review talk given at the International Symposium on Electron and Photon Interactions at High Energies, Bonn, August, 1973. See DESY preprint 73/49.

[2] R. Talman, review talk given at the International Symposium on Electron and Photon Interactions at High Energies, Bonn, August, 1973. See Cornell preprint CLNS-249.

[3] H. Meyer, review talk given at the International Symposium on Electron and Photon Interactions at High Energies, Bonn, August, 1973. See U. C. Santa Cruz preprint 73/011.

[4] A. B. Clegg, review talk given at the International Symposium on Electron and Photon Interactions at High Energies, Bonn, August, 1973.

[5] C. J. Bebek et al., papers submitted to the International Conference on High Energy Physics, London, July, 1974.

[6] P. H. Garbincius et al., *Phys. Rev. Lett.* **32**, 328 (1974); A. J. Sadoff et al., *Phys. Rev. Lett.* **32**, 955 (1974); B. Gibbard et al., *Phys. Rev.* (to be published).

[7] E. D. Bloom, review talk given at the International Symposium on Electron and Photon Interactions at High Energies, Bonn, August, 1973.

[8] C. J. Bebek et al., *Phys. Rev. Lett.* **30**, 624 (1973); *Phys. Rev. Lett.* **32**, 21 (1974); *Phys. Rev. Lett.* **32**, 27 (1974); *Phys. Rev.* **D9**, 1229 (1974); and earlier papers cited in these references.

[9] J. C. Alder et al., *Nucl. Phys.* **B46**, 415 (1972).

[10] C. Driver et al., *Nucl. Phys.* **B30**, 245 (1971); *Nucl. Phys.* **B33**, 84 (1972); *Nucl. Phys.* **B38**, 1 (1972); *Nucl. Phys.* **B39**, 106 (1972). I. Dammann et al., *Nucl. Phys.* **B54**, 381 (1971). T. Azemoon *et al.*, contribution No 116 to the International Symposium on Electron and Photon Interactions at High Energies, Bonn, August, 1973.

[11] A. Sofair et al., *Nucl. Phys.* **B42**, 369 (1972).
[12] E. D. Bloom et al., *Phys. Rev. Lett.* **28**, 516 (1972).
[13] E. Lazarus et al., *Phys. Rev. Lett.* **29**, 743 (1972); *Phys. Rev. Lett.* **29**, 1409 (1972). L. Ahrens et al., *Phys. Rev. Lett.* **31**, 131 (1973); *Phys. Rev.* **D9**, 1894 (1974).
[14] R. Talman et al., data presented in Ref. 2.
[15] J. T. Dakin et al., *Phys. Rev. Lett.* **29**, 746 (1972); *Phys. Rev.* **D8**, 687 (1973).
[16] J. Ballam et al., contribution No 287 to the International Symposium on Electron and Photon Interactions at High Energies, Bonn, August, 1973.
[17] V. Eckhardt et al., *Nucl. Phys.* **B55**, 45 (1973); and DESY preprint 74/5.
[18] F. A. Behrends, R. Gastmans, *Phys. Rev.* **D5**, 204 (1972); R. C. E. Devenish, D. H. Lyth, *Phys. Rev.* **D5**, 47 (1972); R. W. Manweiler, W. Schmidt, *Phys. Rev.* **D3**, 2752 (1971); and other papers cited by these references.
[19] H. Fraas, D. Schildknecht, *Phys. Lett.* **37B**, 389 (1971); F. A. Behrends, R. Gastmans, *Phys. Rev. Lett.* **27**, 124 (1971).
[20] S. D. Drell, D. J. Levy, T. M. Yan, *Phys. Rev. Lett.* **22**, 744 (1969); *Phys. Rev. Lett.* **24**, 855 (1970).
[21] A. Ramanauskas et al., *Phys. Rev. Lett.* **31**, 1371 (1973).